



저작자표시-비영리-변경금지 2.0 대한민국

이용자는 아래의 조건을 따르는 경우에 한하여 자유롭게

- 이 저작물을 복제, 배포, 전송, 전시, 공연 및 방송할 수 있습니다.

다음과 같은 조건을 따라야 합니다:



저작자표시. 귀하는 원저작자를 표시하여야 합니다.



비영리. 귀하는 이 저작물을 영리 목적으로 이용할 수 없습니다.



변경금지. 귀하는 이 저작물을 개작, 변형 또는 가공할 수 없습니다.

- 귀하는, 이 저작물의 재이용이나 배포의 경우, 이 저작물에 적용된 이용허락조건을 명확하게 나타내어야 합니다.
- 저작권자로부터 별도의 허가를 받으면 이러한 조건들은 적용되지 않습니다.

저작권법에 따른 이용자의 권리는 위의 내용에 의하여 영향을 받지 않습니다.

이것은 [이용허락규약\(Legal Code\)](#)을 이해하기 쉽게 요약한 것입니다.

[Disclaimer](#)

Master of Science

**Photocatalytic Hydrogen Evolution over
Platinum-containing Graphitic Carbon Nitride modified by
simple Chemical Oxidation**

The Graduate School of the University of Ulsan

Department of Chemical Engineering

Duc Quang Dao

*Photocatalytic Hydrogen Evolution over
Platinum-containing Graphitic Carbon Nitride modified by
simple Chemical Oxidation*

Supervisor: Professor Eun Woo Shin

A Dissertation

Submitted to

The Graduate School of the University of Ulsan

In partial Fulfillment of the Requirements for the Degree of

Master of Science

by

Duc Quang Dao

Department of Chemical Engineering

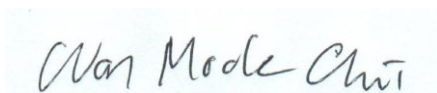
University of Ulsan

Ulsan, South Korea

July 2021

***Photocatalytic Hydrogen Evolution over
Platinum-containing Graphitic Carbon Nitride modified by
simple Chemical Oxidation***

This certifies that the master's thesis of Duc Quang Dao is approved.



Committee Chair Prof. Won Mook Choi



Committee Member Prof. Eun Woo Shin



Committee Member Prof. Sung Gu Kang

Department of Chemical Engineering

University of Ulsan

Ulsan, South Korea

July 2021

ACKNOWLEDGEMENTS

I would like to express my deepest appreciation to my advisor, Professor Eun Woo Shin for not only providing me with firm guidance through all stages of my study but also with valuable and constructive advice on my very first steps toward research life.

I would like to extend my sincere thanks to my committee, Professor Won Mook Choi and Professor Sung Gu Kang for spending their precious time reviewing this dissertation and support this work.

I also had the great pleasure of working with my seniors and present lab mates, Dr. Nguyen Phu Huy, Dr. Do Thi Lien, Ms. Nguyen Thi Kim Anh, Ms. Ming-yan Wang, Mr. Hae-won Jung, Mr. Sang-yoon Kim, and Mr. Nguyen Phuong Anh, and I gratefully acknowledge their wholehearted supports in my researching and living. Besides, I would like to recognize the assistance that I received from Mrs. Kyong Cho Lim and from all of my friends in the Department of Chemical Engineering for helping me use analysis instruments in the department.

Finally, the completion of this dissertation would not have been possible without the support and encouragement from my beloved family.

ABSTRACT

In this study, platinum (Pt)-containing graphitic carbon nitride (g-C₃N₄) catalysts modified using simple chemical oxidation of g-C₃N₄ were prepared for the first time, and the catalysts were applied to photocatalytic hydrogen evolution tests. The hydrogen production rates of the chemically oxidized Pt/g-C₃N₄ photocatalysts (2,471.7 and 3,640.8 $\mu\text{mol g}^{-1} \text{h}^{-1}$) were found to be at least 5 times higher than those of bulk Pt/g-C₃N₄ (429.3 and 728.8 $\mu\text{mol g}^{-1} \text{h}^{-1}$). During the Pt photodeposition on the g-C₃N₄ surface, the chemically oxidized g-C₃N₄ with a more negatively charged surface and the functional groups maintained the high ratio of Pt²⁺/Pt⁰ among the Pt nanoparticles. The higher proportion of Pt²⁺ sites on the chemically oxidized g-C₃N₄ enhanced the hydrogen evolution rate by suppressing the reversible reaction route of H₂ to 2H⁺. In addition, the chemically oxidized g-C₃N₄ with oxygen-containing functional groups improved the separation efficiency of photoexcited charges over Pt/g-C₃N₄.

On the basis of the enhanced hydrogen production thanks to the above-mentioned properties of chemically oxidized g-C₃N₄, different Pt loading methods such as chemical reduction, hydrogen reduction, and photoreduction on chemically oxidized g-C₃N₄ were studied to investigate the support's properties on Pt deposition processes. Among different Pt loading methods, the hydrogen reduction method gave the chemically oxidized Pt/g-C₃N₄ with the highest photocatalytic hydrogen production, which could be explained by the synergy of high ratio of Pt²⁺/Pt⁰, high Pt nanoparticles distribution, and efficient photoinduced charge transfer from chemically oxidized g-C₃N₄ onto active site Pt.

TABLE OF CONTENTS

Acknowledgements	i
Abstract	ii
Table of Contents	iii
List of Figures	iv
List of Tables	vi
Nomenclatures	vii
Chapter 1: Introduction	1
1.1 Global energy crisis and hydrogen energy from water splitting	1
1.2 Pt/g-C ₃ N ₄ photocatalyst and chemical oxidation method	4
1.3 Research objectives.....	5
Chapter 2: Experiments	6
2.1 Catalyst preparation	6
2.1.1 Preparation of bulk and chemically oxidized Pt/g-C ₃ N ₄	6
2.1.2 Different Pt loading methods on g-C ₃ N ₄ support	7
2.2 Characterization	8
2.3 Computational methods	9
2.4 Photocatalytic hydrogen evolution	10
2.4.1 Hydrogen evolution of bulk and chemically oxidized Pt/g-C ₃ N ₄	10
2.4.2 Hydrogen evolution of Pt/g-C ₃ N ₄ with different Pt loading methods	10
Chapter 3: Results and discussion.....	12
3.1 Chemically oxidized Pt/g-C ₃ N ₄	12
3.1.1 Photocatalytic performance evaluation	12
3.1.2 Morphological, physicochemical, and electrical properties	17
3.1.3 Optical properties	33
3.1.4 Origin of photocatalytic activity enhancement.....	36
3.2 Different Pt-loaded g-C ₃ N ₄ photocatalysts	38
3.2.1 Photocatalytic performance evaluation	38
3.2.2 Morphological, physicochemical, and electrical properties	40
3.2.3 Optical properties	49
Chapter 4: Conclusions	52
References	53

LIST OF FIGURES

Figure 1.1. Total global energy consumption since 2000 with projections until 2050 [1].....	1
Figure 1.2. Global greenhouse gas emissions [2]	2
Figure 1.3. Global carbon emissions from fossil fuels, 1900 - 2014 [2]	2
Figure 1.4. Hydrogen production methods	3
Figure 1.5. Photocatalytic water splitting processes on heterogeneous photocatalysts [4].....	4
Figure 2.1. Photocatalysts synthesis schematic	7
Figure 3.1. (A) H ₂ production rates of g-C ₃ N ₄ in comparison with Pt/g-C ₃ N ₄ photocatalysts and (B) cyclic H ₂ production of Pt/AO under solar-simulated irradiation	13
Figure 3.2. Photocatalytic H ₂ production over time and (B) H ₂ production rates of bulk and chemically oxidized Pt/g-C ₃ N ₄ photocatalysts	14
Figure 3.3. Overall photodeposition process of Pt on bulk and chemically oxidized g-C ₃ N ₄	18
Figure 3.4. Nitrogen adsorption–desorption isotherms of Pt/g-C ₃ N ₄ photocatalysts	20
Figure 3.5. FE-SEM images of Pt/g-C ₃ N ₄ photocatalysts	21
Figure 3.6. SEM image of Pt/NB and corresponding EDS element mappings of C, N, and Pt	22
Figure 3.7. HR-TEM images and Pt particle size distribution of (A) Pt/AB, (B) Pt/NB, (C) Pt/AO, and (D) Pt/NO	23
Figure 3.8. (A) XRD patterns and (B) FT-IR spectra of Pt/g-C ₃ N ₄ photocatalysts....	25
Figure 3.9. XPS survey spectra of Pt/g-C ₃ N ₄ photocatalysts	26
Figure 3.10. XPS spectra of C 1s, O 1s, N 1s, and Pt 4f for Pt/g-C ₃ N ₄ photocatalysts	27
Figure 3.11. Different N species in g-C ₃ N ₄ structure	29
Figure 3.12. Zeta potential distribution curves of bulk and chemically oxidized g-C ₃ N ₄	30
Figure 3.13. Relaxed (a) pristine and (b) chemically oxidized g-C ₃ N ₄ . Herein, C, N, O, and H are displayed using brown, light blue, red, and white balls, respectively	31
Figure 3.14. (A) UV–vis absorption spectra, (B) steady-state PL spectra, (C) time-resolved PL spectra, and (D) Nyquist plots of the Pt/g-C ₃ N ₄ photocatalysts	34
Figure 3.15. Tauc plots of Pt/g-C ₃ N ₄ photocatalysts	35

Figure 3.16. Illustration of photocatalytic H ₂ evolution reaction over chemically oxidized Pt/g-C ₃ N ₄	38
Figure 3.17. (A) Cyclic photocatalytic H ₂ production over time and (B) H ₂ production rates and corresponding Pt ²⁺ /Pt ⁰ ratios of Pt/CCN, Pt/HCN, and Pt/PCN photocatalysts	39
Figure 3.18. Nitrogen adsorption–desorption isotherms (inset: pore diameter distribution) of Pt/g-C ₃ N ₄ photocatalysts	41
Figure 3.19. FE-SEM images of Pt/g-C ₃ N ₄ photocatalysts	42
Figure 3.20. FE-TEM images of (A and B) Pt/CCN, (C) Pt/HCN, and (D and E) Pt/PCN.....	43
Figure 3.21. (A) STEM image and (B) corresponding Pt EDS mapping of Pt/HCN.	44
Figure 3.22. (A) AFM image and (B) corresponding cross-sectional profile of Pt/HCN	44
Figure 3.23. (A) XRD patterns and (B) FT-IR spectra of Pt/g-C ₃ N ₄ photocatalysts..	45
Figure 3.24. Hydrazinolysis of g-C ₃ N ₄	45
Figure 3.25. XPS survey spectra of Pt/g-C ₃ N ₄ photocatalysts	47
Figure 3.26. XPS spectra of C 1s, N 1s, O 1s, and Pt 4f for Pt/g-C ₃ N ₄ photocatalysts	48
Figure 3.27. (A) UV–vis absorption spectra, (B) Tauc plots, (C) steady-state PL spectra, (D) time-resolved PL spectra, and (E) Nyquist plots of the Pt/g-C ₃ N ₄ photocatalysts	51

LIST OF TABLES

Table 3.1. H ₂ production activity of Pt/AO in comparison with photodeposited Pt/g-C ₃ N ₄ photocatalysts introduced in 2017–2019	16
Table 3.2. Physicochemical and optical properties of Pt/g-C ₃ N ₄ photocatalysts	19
Table 3.3. Textural properties of the prepared catalysts	19
Table 3.4. O, H, and N contents, N-containing bond percentages, and ratios of Pt phases.....	28
Table 3.5. Bader atomic charge (e) distribution of pristine and doped g-C ₃ N ₄ . Each number corresponds to the number in Figure 3.13	32
Table 3.6. Fluorescence emission lifetime and relevant percentage data fitted using a three-exponential function	35
Table 3.7. Physicochemical and optical properties of Pt/g-C ₃ N ₄ photocatalysts	40
Table 3.8. O 1s XPS analysis results	49
Table 3.9. Pt species and corresponding H ₂ production rates of Pt/g-C ₃ N ₄ photocatalysts	49

NOMENCLATURES

Abbreviations

EA	Elemental analysis
EDS	Energy Dispersive X-ray spectra
EIS	Electrochemical Impedance Spectroscopy
FE-SEM	Field Emission Scanning Electron Microscopy
FT-IR	Fourier Transform Infrared Spectra
HR-TEM	High Resolution Transmission Electron Microscopy
ICP-OES	Inductively coupled plasma - optical emission spectrometry
LED	Light emitting diode
TOF	Turnover frequency
UV-Vis	Ultraviolet – visible
XPS	X-ray Photoelectron Spectroscopy
XRD	X-ray Diffraction

Roman and Greek letters

E_g	Optical and gap energy (eV)
d	Average crystallite size (nm)
S_{BET}	Specific surface area (m^2/g)
λ	Wavelength (nm)

Chapter 1: Introduction

This chapter outlines the need for hydrogen energy, water splitting process (section 1.1), Pt/g-C₃N₄ photocatalyst, and chemical oxidation method (section 1.2). Finally, section 1.3 describes the purposes of this research.

1.1 Global energy crisis and hydrogen energy from water splitting

The rapid climb in the world population and higher lifestyle standards have led to tremendous growth in global energy demand. Figure 1.1 displays energy consumption in the world from 2000 with a projection to 2050. There is an upward trend from the beginning of this century, and this trend is predicted to continue up to and including 2030.

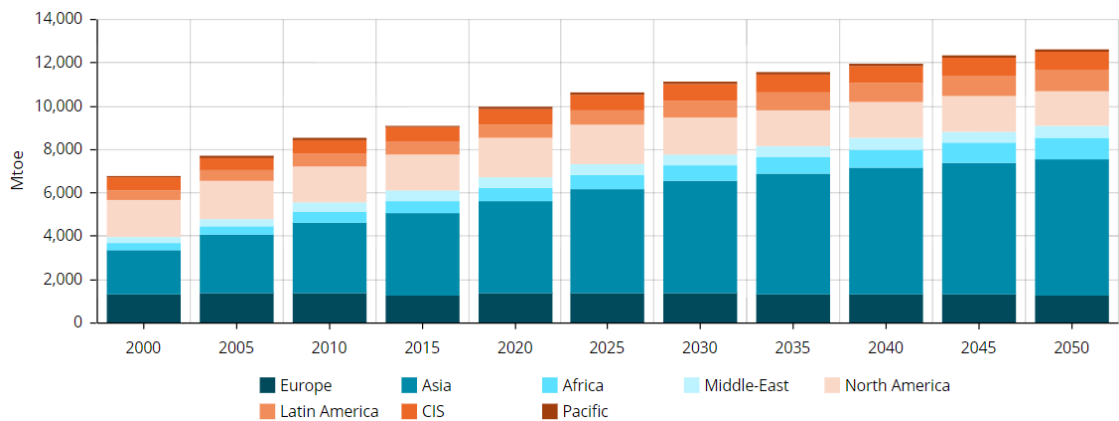


Figure 1.1. Total global energy consumption since 2000 with projections until 2050 [1]

Along with higher energy consumption is the higher greenhouse gas emission, in which CO₂ takes part in over 3 fourth mainly from fossil fuels (see Figure 1.2 and 1.3). Greenhouse gas emission has been one of the main reasons for the Earth's climate change by trapping heat, and also contributed to respiratory disease from smog and air pollution. Extreme weather, food supply disruptions, and increased wildfires are other effects of climate change caused by greenhouse gases.

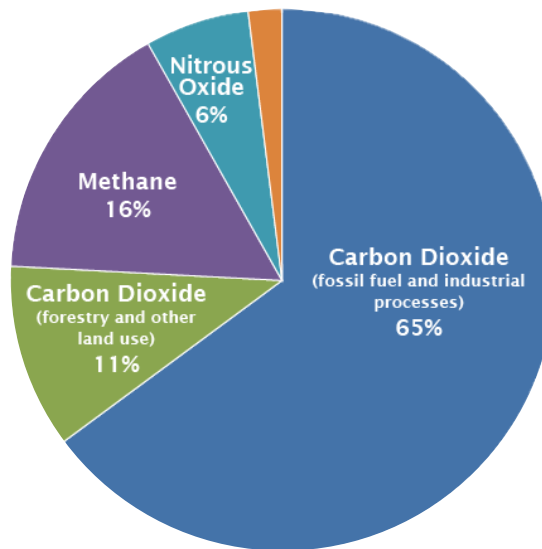


Figure 1.2. Global greenhouse gas emissions [2]

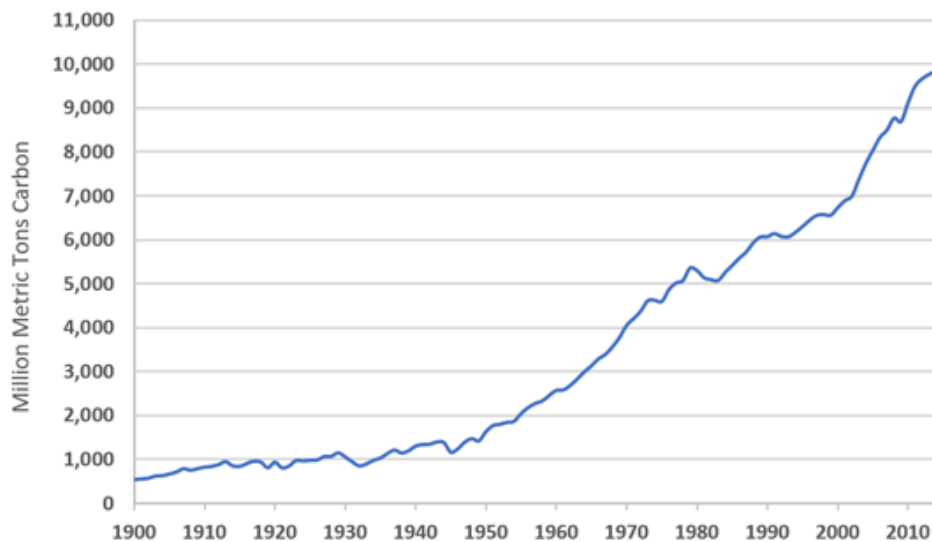


Figure 1.3. Global carbon emissions from fossil fuels, 1900 - 2014 [2]

Therefore, there is an urgent need for the development of an alternative energy resource to fossil fuels that is renewable, clean, and environment friendly to help overcome present global issues including climate emergency, eventual exhaustion of energy supplies, retail uncertainty, and foreign oil reliance. Nowadays, there are several alternative energy sources including wind, geothermal, hydropower, and solar which are relatively clean and sustainable in comparison with fossil fuels, however, each of them has some limitations which make this substitution challenging:

- Electricity producing from wind turbines is not storable and the wind turbines themselves are dangerous with nearby residents.

- Geothermal energy requires a high cost to be practical and may lead to geological instability.
- Hydroelectric energy brings about many environmental issues like deforestation, methane gas from dead trees, and interruption to wildlife. Besides, it is known to be potential for dam failure.
- Although solar energy is free, it has some drawbacks due to the dependence on location and time, and the low energy density per unit land area.

Hydrogen (H_2) is considered to be a storable and clean energy source for the future. The main advantages of using hydrogen as a fuel include its sustainable sources like biomass or water, its high energy yield, its friendly with the environment, and its high storage capability.

There are two main pathways to produce H_2 today (Figure 1.4). Comparing with other resources for H_2 production, water is the most inexpensive and plentiful on the Earth. Furthermore, among the sustainable energies, solar energy has been considered a more promising source due to its lesser location dependence in comparison to wind and hydropower energy. Therefore, H_2 production by photocatalytic water splitting has attracted great interest because of its applicability in the conversion of abundant solar energy to clean hydrogen energy, enabling sustainable development via semiconductor photocatalysis technology [3]. Besides the low cost and high solar-to- H_2 efficiency, this method can separate hydrogen and oxygen streams and can be applied in various reactor sizes which is appropriate for small-scale usage.

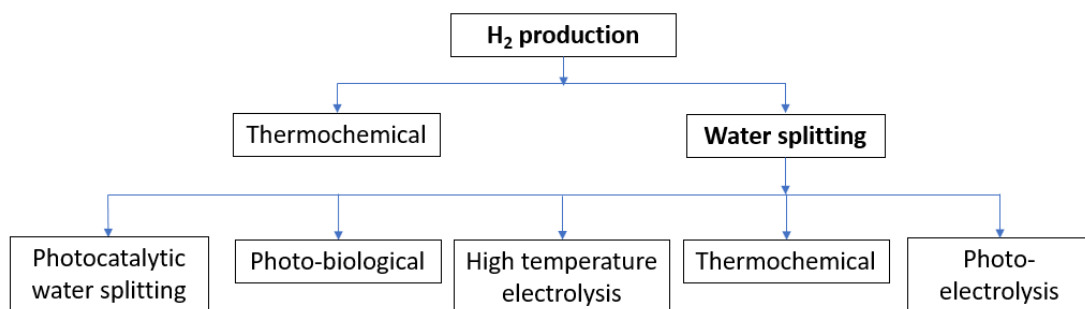


Figure 1.4. Hydrogen production methods

The photocatalytic water splitting process is described in Figure 1.5 [4]:

- In the first step, the photocatalyst absorbs photon energy higher than its band gap energy and generates excited electrons and holes.

- Then, these photoexcited charges separate and move to the surface of the catalyst.
- In the last step, the adsorbed water molecules undergo reduction and oxidation by reaction with the photogenerated electrons and holes to produce H_2 and O_2 , respectively.

The first two steps depend strongly on the structural and electronic properties of the semiconductor photocatalyst, while the third step is promoted by a cocatalyst loaded on the photocatalyst surface, which usually is a noble metal such as Platinum (Pt) or Palladium (Pd).

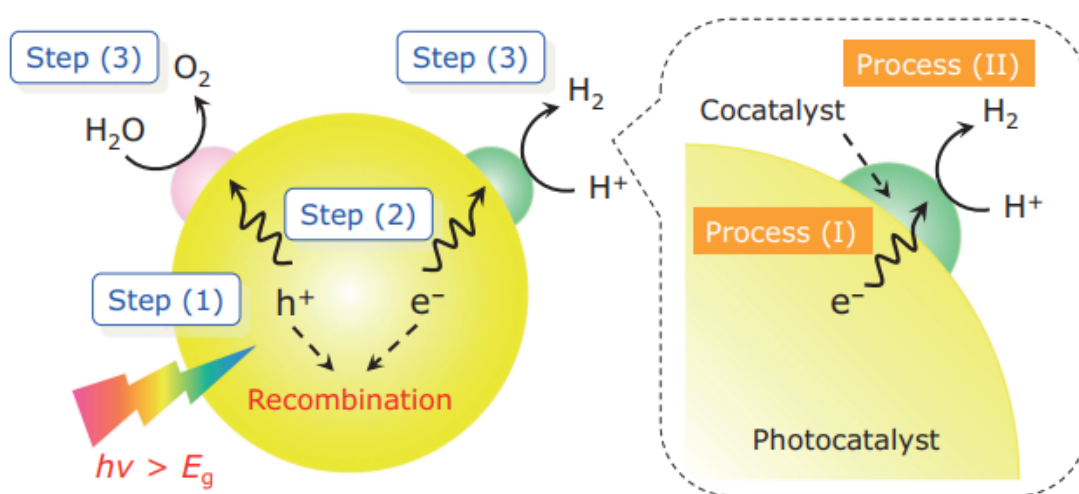


Figure 1.5. Photocatalytic water splitting processes on heterogeneous photocatalysts [4]

1.2 Pt/g-C₃N₄ photocatalyst and chemical oxidation method

The high efficiency of semiconductor photocatalysis is the key to advance solar energy harvesting into feasible industrial applications [5]. Even though a lot of semiconductor photocatalysts have been extensively investigated, graphitic carbon nitride (g-C₃N₄), a metal-free polymeric semiconductor, has been paid special attention to in recent years owing to a narrow bandgap (2.7 eV) fitted to visible light irradiation, a simple preparation way to large-scale production, and surface functional groups to improve the photocatalytic performance [6, 7]. However, g-C₃N₄ as a photocatalyst has a limit from its three-dimensional layered structure that significantly hinders electron transportation in g-C₃N₄ and fast recombination of photo-induced electron-hole pairs, thus resulting in a decrease of the photocatalytic activity [8-10]. In the past decade, many efforts have been made to overcome the disadvantages of g-C₃N₄ [11-15].

Recently, chemical oxidation in a $\text{K}_2\text{Cr}_2\text{O}_7/\text{H}_2\text{SO}_4$ solution of g- C_3N_4 was introduced to modify the surface properties of g- C_3N_4 [16, 17]. The chemical oxidation of g- C_3N_4 can cause the exfoliation of C_3N_4 sheets from the three-dimensional g- C_3N_4 structure and the formation of functional groups on the g- C_3N_4 surface, which is advantageous approach to promote the photocatalytic efficiency of g- C_3N_4 . In a previous study, the introduction of functional groups onto the exfoliated C_3N_4 sheets in the chemical oxidation step increased the adsorption capacity and photocatalytic activity of chemically oxidized g- C_3N_4 [17]. Another promising way to enhance the photocatalytic hydrogen evolution performance over g- C_3N_4 is to use a noble metal as a co-catalyst. Specifically, the role of Pt co-catalyst in the photocatalytic hydrogen evolution has been widely studied in abundant literature because Pt is one of the most efficient co-catalysts in the photocatalytic processes [3, 18-22]. To date, there have been several important issues in the utilization of Pt as co-catalyst to improve the photocatalytic hydrogen evolution rate: i) Pt nanoparticle size effect [20, 23], ii) metal-support interaction [19, 24], and iii) active Pt sites on hydrogen evolution [18, 25-27].

However, to the best of our knowledge, Pt co-catalyst has not been loaded into the g- C_3N_4 modified by the simple chemical oxidation and this system has not been employed for photocatalytic hydrogen evolution, yet. The features of the chemically oxidized g- C_3N_4 such as the exfoliated g- C_3N_4 morphology containing surface functional groups can induce unique interaction with the Pt co-catalyst during the different Pt loading processes, thus resulting in high efficiency of photocatalytic hydrogen evolution.

1.3 Research objectives

In the scope of this thesis, novel Pt/g- C_3N_4 photocatalysts prepared by the simple chemical oxidation to apply for the photocatalytic water splitting were synthesized for the first time. The photocatalytic hydrogen evolution performances of the chemically oxidized Pt/g- C_3N_4 were investigated compared with those of bulk Pt/g- C_3N_4 . Based on the enhancement in photocatalytic activity and correlatively important properties such as Pt particle size, Pt oxidative states, g- C_3N_4 surface functional groups, g- C_3N_4 surface charge, and photo-excited electron-hole pairs separation efficiency, different Pt loading methods on chemically oxidized Pt/g- C_3N_4 (chemical reduction, hydrogen reduction, and photoreduction) were conducted to study the influence of these properties on efficiency of hydrogen evolution by various state-of-the-art characterization methods.

Chapter 2: Experiments

2.1 Catalyst preparation

2.1.1 Preparation of bulk and chemically oxidized Pt/g-C₃N₄

The preparation of bulk and chemically oxidized Pt/g-C₃N₄ photocatalysts is described in Figure 2.1.

Synthesis of bulk g-C₃N₄

Bulk g-C₃N₄ was synthesized from thiourea (CH₄N₂S) in different calcination atmospheres (air and nitrogen) following this procedure. Briefly, 6 g of the precursor was added into an Al-foil-covered crucible, which was placed in an oven and heated to 500°C at a ramping rate of 5°C/min; this was followed by calcination at 500°C for four hours in the air. The same procedure was repeated under N₂ calcination atmospheres without Al foil covering. The obtained yellow agglomerates were ground into powder for further treatment. The bulk g-C₃N₄ powders prepared under the calcination atmospheres of air and nitrogen (N₂) were named AB and NB, respectively.

Synthesis of chemically oxidized g-C₃N₄

Chemically oxidized g-C₃N₄ photocatalysts were prepared from the bulk g-C₃N₄ powders via chemical oxidation according to the method described in the previous study [17]. In brief, 10 g of K₂Cr₂O₇ and 50 mL of H₂SO₄ were mixed in a 100-mL flask using a magnetic stirrer at 20 °C for 40 min, at which point the solution had turned brown. Then, 0.5 g of bulk g-C₃N₄ powder was added to the solution, and the solution was stirred continuously for 1 h to achieve the chemical oxidation of g-C₃N₄. Next, the solution was slowly poured into 500 mL of DI water and left to naturally cool down to room temperature. Afterward, the acidic solution was washed several times with DI water using centrifugation and sonication to remove all the residual components. Finally, the undispersed g-C₃N₄ was separated via centrifugation from the milk-like solution, whose solid/liquid ratio was later adjusted to a concentration of 5 mg/mL. The chemically oxidized g-C₃N₄ photocatalysts were labeled AO and NO, corresponding to the bulk g-C₃N₄ synthesized in air and N₂ calcination atmospheres, respectively.

Synthesis of Pt-loaded g-C₃N₄

In 90 mL of DI water, 50 mg of g-C₃N₄ was dispersed via 30 min of magnetic stirring. Then, 10 mL of Pt-precursor H₂PtCl₆ solution was added, with the initial Pt content calculated as 3 wt.%. After 10 min of purging with pure argon (Ar) flow, the photodeposition of Pt as a co-catalyst on g-C₃N₄ was undertaken in this system via 60 min of solar-simulated irradiation. Finally, the precipitates were washed with DI water several times and freeze-dried for collection and further characterization. The obtained catalysts were labeled Pt/AB, Pt/NB, Pt/AO, and Pt/NO, corresponding to their g-C₃N₄ parents, respectively.

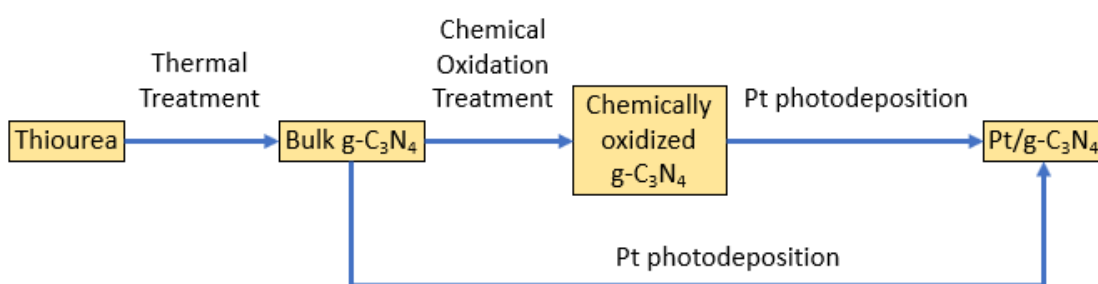


Figure 2.1. Photocatalysts synthesis schematic

2.1.2 Different Pt loading methods on g-C₃N₄ support

In the following section, chemically oxidized g-C₃N₄ synthesized in the air (AO) was used as support to investigate three different Pt loading methods on g-C₃N₄: chemical reduction, hydrogen reduction, and photoreduction. The Pt contents were calculated and kept at 3 wt% in all experiments.

Chemical reduction method:

Chemically oxidized g-C₃N₄ (AO) with a content of 0.5 mg/mL was dispersed with H₂PtCl₆ in DI water, and the solution temperature was slowly increased to 40 °C. Then, hydrazine (N₂H₂) solution with the mole ratio of N₂H₂ : Pt = 1.1 : 1 was added to the mixture, and the reduction was carried on by stirring in 1 h. Finally, the precipitate was washed with DI water several times and freeze-dried for collection and further characterization. The obtained catalyst was labeled Pt/CCN.

Hydrogen reduction method:

Chemically oxidized g-C₃N₄ (AO) with a content of 0.5 mg/mL was dispersed with H₂PtCl₆ in DI water by stirring in a 200-mL 3 necks flask, and the solution temperature was slowly increased to 60 °C. Simultaneously, H₂ flow was purged into the

solution with the flow rate of 25 mL/min, and the reduction was carried on in 50 min. Finally, the precipitate was washed with DI water several times and freeze-dried for collection and further characterization. The obtained catalyst was labeled Pt/HCN.

Photoreduction method:

In 90 mL of DI water, 50 mg of AO was dispersed via 30 min of magnetic stirring. Then, 10 mL of Pt-precursor H_2PtCl_6 solution was added, with the initial Pt content calculated as 3 wt.%. After 10 min of purging with pure argon (Ar) flow, the photodeposition of Pt on AO was undertaken in this system via 60 min of solar-simulated irradiation. Finally, the precipitates were washed with DI water several times and freeze-dried for collection and further characterization. The obtained catalysts were labeled Pt/PCN.

2.2 Characterization

The content of Pt elements in the as-prepared samples was analyzed by an inductively coupled plasma-optical emission spectrometer (ICP-OES; 700-ES Varian, Mulgrave, Australia). The specific surface area and other porosity properties of the samples were measured via N_2 adsorption isotherm processes using a QUADRASORBTM SI Surface Area and Pore Size Analyzer (Quantachrome Instrument, Boynton Beach, FL, U.S.A.). The morphologies of all photocatalyst samples were analyzed by field-emission scanning electron microscopy (FE-SEM; JSM-6500 JEOL, Tokyo, Japan). The microstructure and the distribution of Pt nanoparticles were examined by high-resolution transmission electron microscopy (HR-TEM; JEL-2100F JEOL, Tokyo, Japan). X-ray diffraction (XRD; Rigaku D/MAZX 2500 V/PC high-power diffractometer, Tokyo, Japan) with a $\text{Cu K}\alpha$ X-ray source operating at a wavelength of $\lambda = 1.5415 \text{ \AA}$ was used to determine the crystalline structures of the obtained samples in the range of 10° – 90° at a scan rate of $2^\circ (2\theta)/\text{min}$. Functional groups of the prepared photocatalysts were characterized with a Fourier transform infrared (FT-IR; Nicolet 380 spectrometer, Thermo Scientific Nicolet iS5 with an iD1 transmission accessory, Waltham, MA, U.S.A.). Elemental compositions, chemical states, and electronic states of the elements were examined by X-ray photoelectron spectroscopy (XPS; Thermo Scientific K-Alpha system, Waltham, MA, USA). Zeta potential analysis was carried out using a zeta potential analyzer (Zetasizer Nano ZS, Malvern Panalytical, Malvern, United Kingdom).

The optical properties of the photocatalysts were analyzed by ultraviolet–visible diffuse reflectance (UV–Vis; SPECORD 210 Plus spectroscope, Analytik Jena, Germany) and photoluminescence measurements (PL; Agilent Cary Eclipse fluorescence spectrophotometer, Santa Clara, CA, U.S.A.) at room temperature with a 473-nm diode laser. Electrochemical impedance spectroscopy measurements were conducted with the use of an impedance analyzer (EIS; VSP BioLogic Science Instruments, Seyssinet–Pariset, France) over a frequency range from 100 kHz to 0.01 Hz, at an amplitude of 10 mV, and a direct current potential of +0.8 VSCE after a 10-min delay. The samples were prepared by dispersing 20 mg of photocatalyst and 2 g of activated carbon into a mixture of 100 μ L of isopropanol 99.7% (Sigma-Aldrich Korea, Gyeonggi, South Korea) and 30 μ L of Nafion 5 wt% (Sigma-Aldrich Korea, Gyeonggi, South Korea). Then, 10 ml of a 1 M sodium hydroxide (NaOH) solution was used as the electrolyte for the three-electrode system. A 6-mm standard-type glassy carbon electrode onto which 10 μ L of the sample was dropped was used as the working electrode. A RE-1BP (Ag/AgCl) electrode was used as the reference electrode, and a platinum wire was used as the counter electrode. The electrodes and SVC-3 voltammetry cell were obtained from ALS Co., Ltd. (Tokyo, Japan). For further confirmation of the photo-excited charge separation efficiency, time-resolved fluorescence spectra were collected under 400-nm laser excitation by a FS5 spectrofluorometer (Edinburgh Instruments Ltd, Livingston, UK) using emission decay profiles and fitted by triexponential functions. Qualitative analysis of C, H, O, and N elements was conducted by Elemental Analyzer (EA; Flash 2000 Thermal Fisher Scientific, Seoul, Korea).

2.3 Computational methods

All plane-wave calculations based on density functional theory (DFT) were done with the VASP code [28, 29], using a GGA–PBE functional [30]. The force and energy convergence thresholds were 0.01 eV/Å and 1×10^{-4} eV, respectively. The cut-off energy used in all calculations was 400 eV. The Monkhorst-Pack [31] k -points of (2,2,6) were employed for pristine and chemically oxidized g-C₃N₄. The supercell used in this study for pristine g-C₃N₄ consists of 96 C atoms and 128 N atoms. Van der Waals interactions were corrected through the DFT–D3 approach [32–35]. Using Bader charge analysis [36, 37], distributions of net atomic charges were revealed for both systems.

2.4 Photocatalytic hydrogen evolution

2.4.1 Hydrogen evolution of bulk and chemically oxidized Pt/g-C₃N₄

The photocatalytic H₂ production experiments were conducted in a quartz flask (inner volume, 300 mL; diameter, 70 mm; and height, 80 mm) surrounded by a water jacket to keep the system working at room temperature. A high-purity flow of Ar was blown through the system during the process to completely remove other impurity gases. A 300-W mercury lamp without any filter was used as the light source for solar simulation. The focused intensity on the solution was 43 mW cm⁻². Specifically, 50 mg of the g-C₃N₄ was dispersed in 80 mL of DI water via magnetic stirring for 30 min. Afterward, 10 mL of H₂PtCl₆ solution was added, with the initial Pt content calculated as 3wt.%. After 10 min of purging by Ar, *in situ* photodeposition of Pt as a co-catalyst was performed in the system under solar-simulated irradiation for 60 min. Finally, 10 mL of TEOA solution was added to the system as a sacrificial reagent, and the system was again evacuated with high-purity Ar gas before the hydrogen production was begun under full-range irradiation. The H₂ production content was measured using an online gas chromatograph with a thermal conductivity detector.

The cycling experiments were carried out under the same conditions using 3-h cycles. At the beginning of every cycle, 10 mL of TEOA was added to the solution, and the system was purged with pure Ar for 10 min.

2.4.2 Hydrogen evolution of Pt/g-C₃N₄ with different Pt loading methods

The photocatalytic H₂ production experiments were conducted similarly to section 2.5.1, except that a LED lamp (400 - 1,100 nm) was used as the light source for solar simulation. The focused intensity on the solution was 1 Sun (100 mW cm⁻²). Specifically, 50 mg of the g-C₃N₄ was dispersed in 90 mL of DI water via magnetic stirring for 30 min. After 20 min of purging by Ar, 10 mL of TEOA solution was added to the system as a sacrificial reagent, and the system was again evacuated with high-purity Ar gas before the hydrogen production was begun under full-range irradiation. The H₂ production content was measured using an online gas chromatograph with a thermal conductivity detector.

The cycling experiments were carried out under the same conditions using 6-h cycles. At the beginning of every cycle, 10 mL of TEOA was added to the solution, and the system was purged with pure Ar for 20 min.

Chapter 3: Results and discussion

3.1 Chemically oxidized Pt/g-C₃N₄

3.1.1 Photocatalytic performance evaluation

Photocatalytic H₂ production based on the water splitting process of as-prepared g-C₃N₄ and Pt/g-C₃N₄ photocatalysts was performed in a 100-mL solution containing 10 vol.% TEOA as a hole sacrificial agent under a full-spectrum solar-simulated irradiation system. The pure bulk g-C₃N₄ samples prepared in air and N₂ atmosphere (AB and NB, respectively) were found to produce up to 59 μmol H₂ per gram catalyst in 1 h (μmol g⁻¹ h⁻¹). The production of chemically oxidized g-C₃N₄ samples (AO and NO) was 239 μmol g⁻¹ h⁻¹ (see Figure 3.1A), indicating that the chemical oxidation method implemented according to our previous report improved the photocatalytic activity of g-C₃N₄ [17]. Importantly, the results demonstrate that the loading of Pt as a noble-metal co-catalyst remarkably enhanced the average H₂ production rates of all bare g-C₃N₄ samples by nearly 13 or 16 times, undeniably confirming the role of Pt in the hydrogen evolution reaction. The stability of chemically oxidized samples was further investigated, and the results of a recycling test on Pt/AO are shown in Figure 3.1B. There was no significant drop in H₂ production activity, revealing the superior photostability of the obtained Pt/AO throughout the 9 h of reaction time.

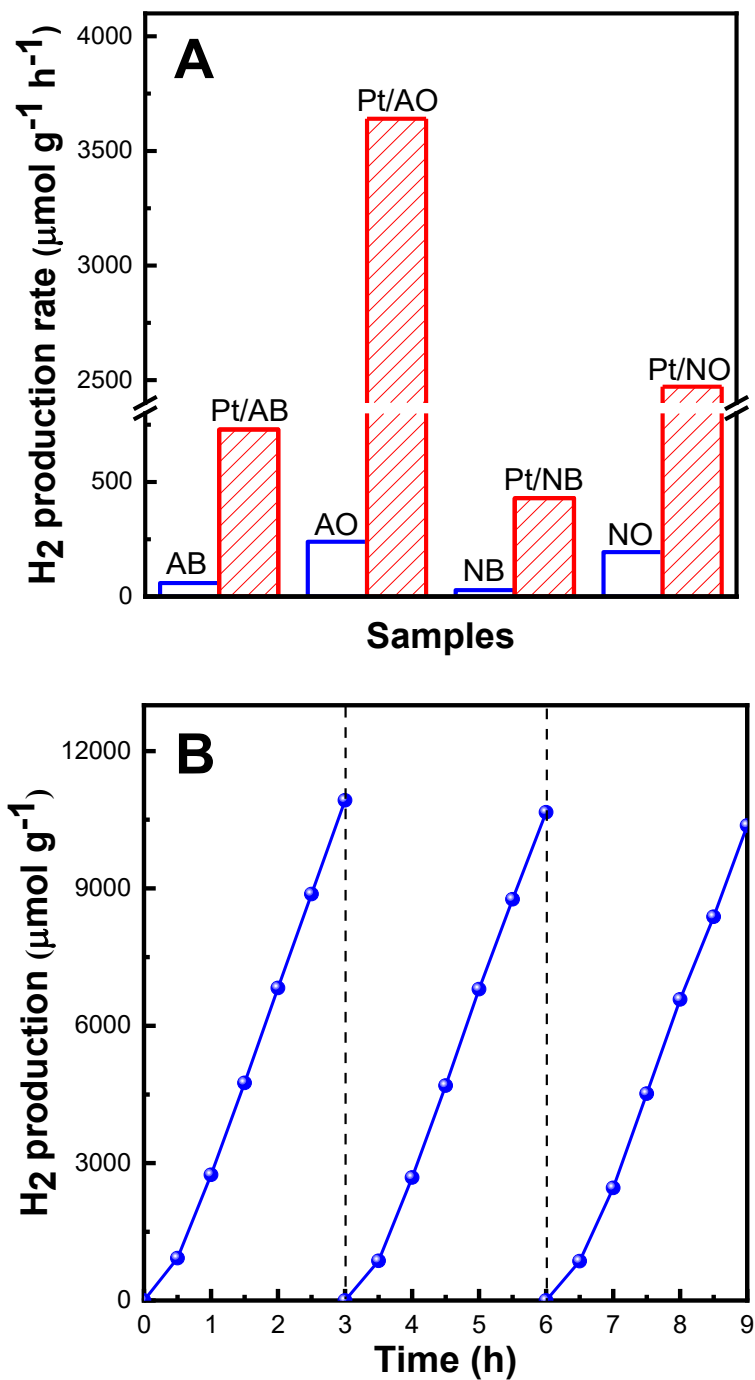


Figure 3.1. (A) H₂ production rates of g-C₃N₄ in comparison with Pt/g-C₃N₄ photocatalysts and (B) cyclic H₂ production of Pt/AO under solar-simulated irradiation

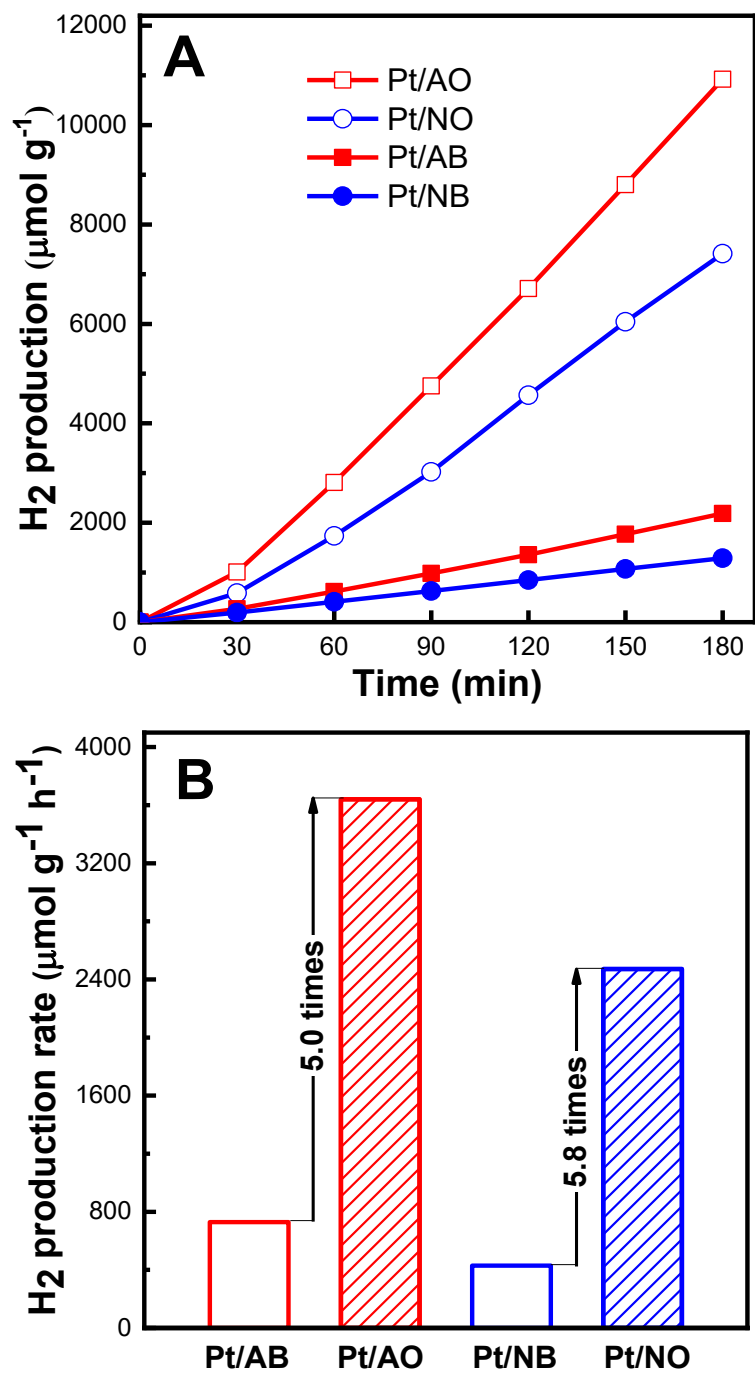


Figure 3.2. Photocatalytic H₂ production over time and (B) H₂ production rates of bulk and chemically oxidized Pt/g-C₃N₄ photocatalysts

As shown in Figure 3.2A, after 3 h of irradiation, Pt/AO and Pt/NO exhibited outstanding H₂ production amounts (10,992 and 7,415 μmol g⁻¹, respectively) when compared with Pt/AB (2,186 μmol g⁻¹) and Pt/NB (1,287 μmol g⁻¹). Additionally, the calculated average H₂ production rates in Figure 3.2B show that the chemical oxidation was able to improve the H₂ production mass activity of Pt/AB by 5 times (from 728.8 to 3,640.8 μmol g⁻¹ h⁻¹ for Pt/AO) and that of Pt/NB by 5.8 times (from 429.3 to 2471.7 μmol g⁻¹ h⁻¹ for Pt/NO).

Table 3.1 compares the H₂ production rates and relative improvement factors of different Pt/g-C₃N₄ photocatalysts prepared by the photodeposition method in recently published studies. With regard to modifying the g-C₃N₄ support properties [38-42] and the properties of the loaded Pt [19, 20], the chemical oxidation method presented in this paper using a mixture of H₂SO₄/K₂Cr₂O₇ is not only simple to conduct but also leads to relatively high photocatalytic H₂ production activity and a middling enhancement factor. This indicates that the developed strategy is a simple and effective method for redesigning bulk g-C₃N₄ prior to loading Pt to create an efficient catalyst for photocatalytic H₂ evolution reaction.

Table 3.1. H₂ production activity of Pt/AO in comparison with photodeposited Pt/g-C₃N₄ photocatalysts introduced in 2017–2019

Catalysts	Treatment methods	H ₂ production ($\mu\text{mol g}^{-1} \text{h}^{-1}$)	Enhancement factor	References
Pt/g-C ₃ N ₄	Oxidation with HNO ₃ of g-C ₃ N ₄	870	16.7	[38]
Pt/g-C ₃ N ₄	Solvothermal treatment of g-C ₃ N ₄	1316.3	20	[39]
Pt/g-C ₃ N ₄	Thermal oxidation with oxygen of g-C ₃ N ₄	1430.1	4.3	[40]
Pt/g-C ₃ N ₄	Thermal oxidation with the aid of isopropanol	1501	3	[41]
Pt/g-C ₃ N ₄	Chemical oxidation with H ₂ SO ₄ /K ₂ Cr ₂ O ₇ of g-C ₃ N ₄	3640.8	5	This work
Pt/g-C ₃ N ₄	Two-step calcination (in argon and air) of g-C ₃ N ₄	5261	8.1	[42]
Pt/g-C ₃ N ₄	Photodeposition of single Pt atom	79	-	[20]
Pt/g-C ₃ N ₄	Photodeposition of single Pt atom at sub-zero temperature	3020	4.3	[19]

3.1.2 Morphological, physicochemical, and electrical properties

The Pt-loaded bulk (Pt/AB and Pt/NB) and chemically oxidized (Pt/AO and Pt/NO) g-C₃N₄ were prepared following the procedure shown in Figure 3.3. Based on ICP-OES measurements, the Pt contents in Pt/AB, Pt/NB, Pt/AO, and Pt/NO were found to be 2.72%, 2.96%, 2.68%, and 2.51%, respectively (Table 3.2), representing quite similar amounts. The textural properties of the prepared catalysts, such as the specific surface area (S_{BET}) and pore volume, are presented in Table 3.3. The chemically oxidized Pt/g-C₃N₄ samples exhibited higher S_{BET} and higher average pore size compared with the bulk Pt/g-C₃N₄ samples despite showing no significant change in total pore volume. The corresponding N₂ adsorption–desorption isotherms of the Pt/g-C₃N₄ materials are shown in Figure 3.4. According to Brunauer–Deming–Deming–Teller classification, all of the samples exhibited type-IV isotherms with an H3 hysteresis loop, implying that the prepared materials were mesoporous solids possessing nanosheet structures [19, 20]. The density of Pt particles covering the g-C₃N₄ surface was calculated based on the Pt content and the measured S_{BET} , as shown in Table 3.2. These values were higher for Pt/AB (0.74 mg m⁻²) and Pt/NB (2.04 mg m⁻²) than for Pt/AO (0.65 mg m⁻²) and Pt/NO (1.06 mg m⁻²), indicating that there was an aggregation of Pt sites on the chemically oxidized g-C₃N₄, which is consistent with the HR-TEM results obtained in this work.

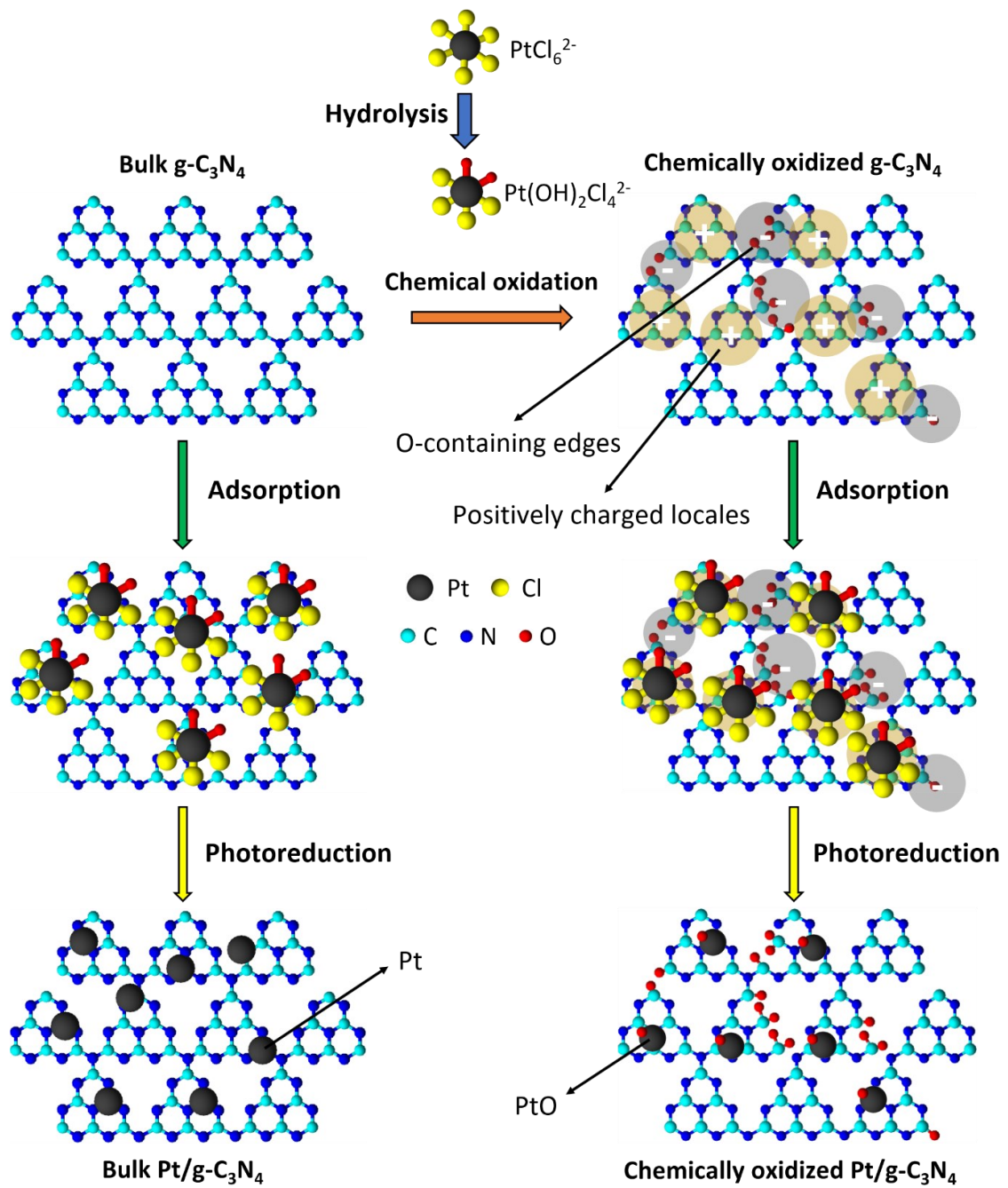


Figure 3.3. Overall photodeposition process of Pt on bulk and chemically oxidized g-C₃N₄.

Table 3.2. Physicochemical and optical properties of Pt/g-C₃N₄ photocatalysts

Sample	Pt content (wt.%) ^a	Covering density (mg m ⁻²) ^b	Pt average size (nm) ^c	d (002) (nm) ^d	Bandgap (eV) ^e
Pt/AB	2.72	0.74	1.28	0.79	2.58
Pt/NB	2.96	2.04	1.95	0.36	2.71
Pt/AO	2.68	0.65	3.2	0.27	2.80
Pt/NO	2.51	1.06	10.6	0.24	3.02

^a Platinum contents were defined using ICP-OES.

^b Covering density (mg m⁻²) = Pt content (wt.%) / 100 × 1 g/S_{BET} (m² g⁻¹) × 1000 mg g⁻¹.

^c Estimated average platinum particle sizes were obtained from TEM images.

^d Interplanar crystal spacing was estimated using the Scherrer equation.

^e Estimated band gaps were obtained from UV–Vis spectra.

Table 3.3. Textural properties of the prepared catalysts

Sample	S _{BET} (m ² /g) ^a	V (cm ³ /g) ^a	L (nm) ^a
Pt/AB	36.603	0.254	27.8
Pt/NB	14.481	0.215	24.2
Pt/AO	41.455	0.250	59.2
Pt/NO	23.610	0.241	42.2

^a Specific surface area (S_{BET}), pore volume (V), and average pore size (L) were determined via N₂ adsorption–desorption isotherm measurements.

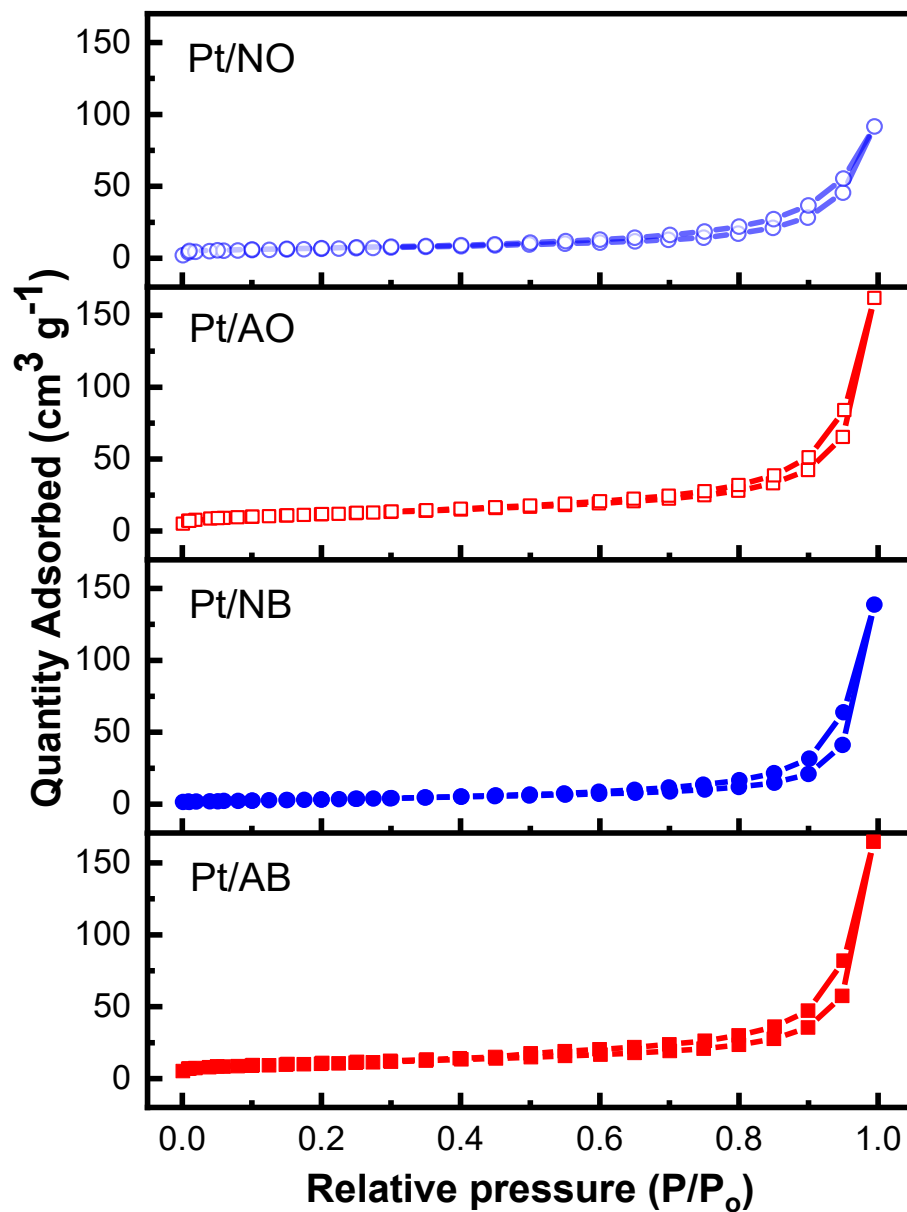


Figure 3.4. Nitrogen adsorption–desorption isotherms of Pt/g-C₃N₄ photocatalysts

The surface morphologies of the Pt/AB, Pt/NB, Pt/AO, and Pt/NO samples were characterized using SEM and TEM, and the results are shown in Figures 3.5 and 3.7, respectively. The SEM image and the corresponding EDS element mappings of Pt/NB (the sample with the highest Pt coverage density in this work) illustrate the high dispersion of Pt along with C and N over the sample's surface (Figure 3.6). Simultaneously, the HR-TEM images (Figure 3.7) clearly demonstrate that the average size of Pt particles or clusters deposited on the chemically oxidized g-C₃N₄ materials was larger than that deposited on the bulk g-C₃N₄. Nevertheless, the remarkable increase in H₂ production of Pt/AO and Pt/NO over Pt/AB and Pt/NB indicates that, within a range of several nanometers, the Pt particle size is not a decisive factor in the photocatalytic activity, which is consistent with previous reports [27, 43]. Besides, in the high-magnification images in Figure 2, lattice fringes characteristic of Pt⁰ (0.23 nm) and PtO (0.27 nm) can be observed in all four samples [44]. These phenomena will be expounded later.

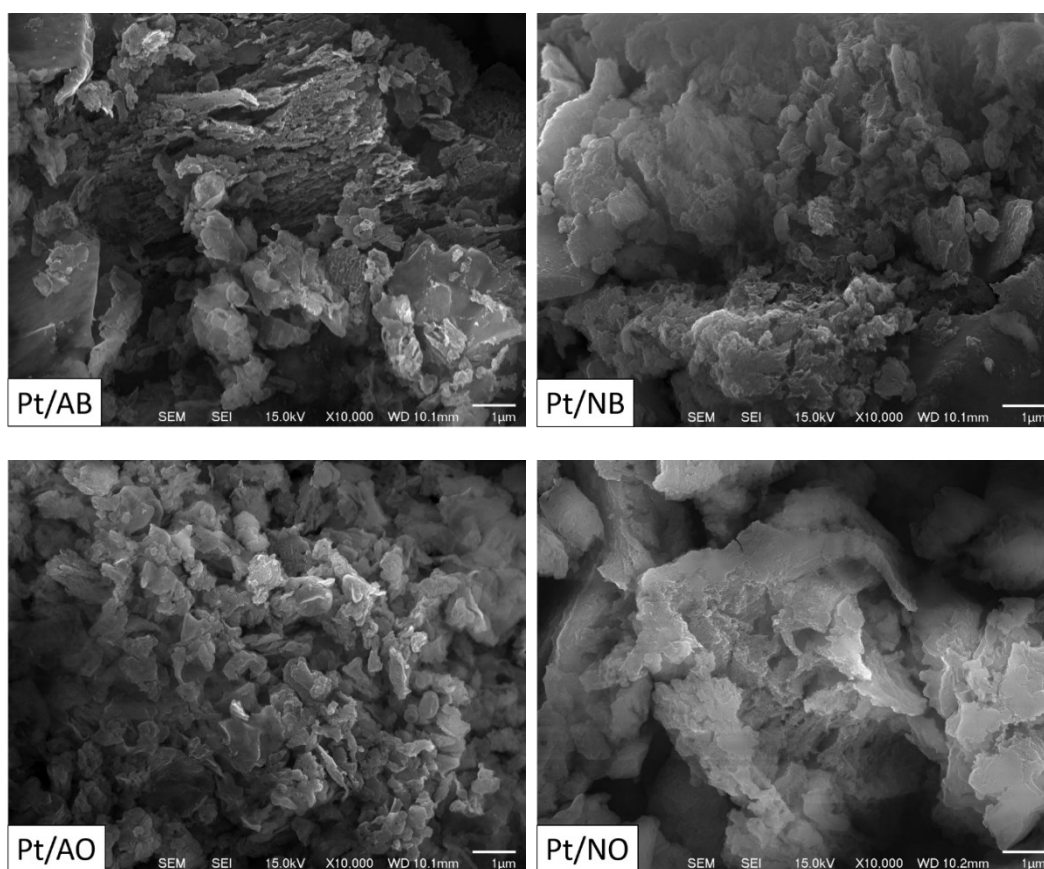


Figure 3.5. FE-SEM images of Pt/g-C₃N₄ photocatalysts

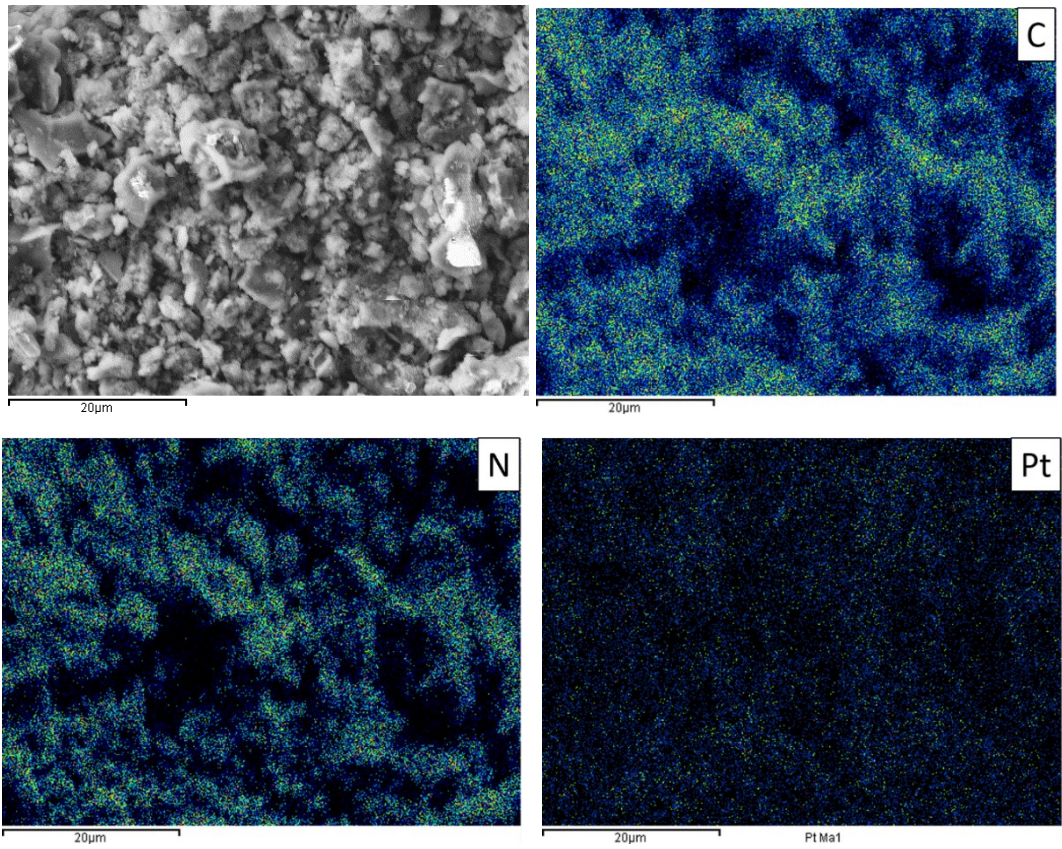


Figure 3.6. SEM image of Pt/NB and corresponding EDS element mappings of C, N, and Pt

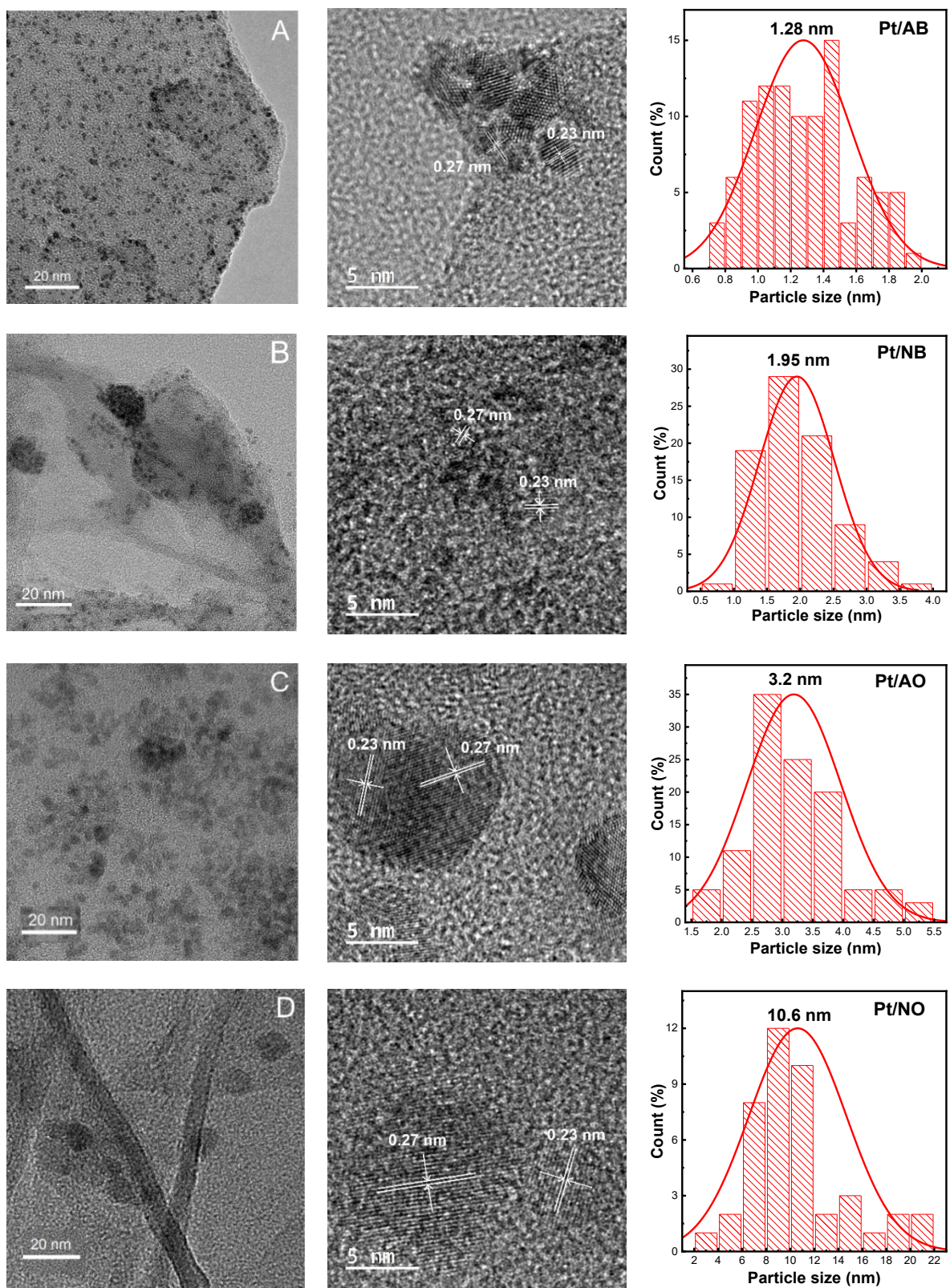


Figure 3.7. HR-TEM images and Pt particle size distribution of (A) Pt/AB, (B) Pt/NB, (C) Pt/AO, and (D) Pt/NO

Figure 3.8A displays the XRD spectra of the bulk (Pt/AB and Pt/NB) and chemically oxidized (Pt/AO and Pt/NO) samples. In all the samples, there were two main characteristic peaks at $2\theta = 12.5^\circ$ and 27.2° , corresponding to the (100) and (002) planes of pure g-C₃N₄, respectively. The former can be ascribed to the in-plane packing of a tri-s-triazine structure, whereas the latter corresponds to interlayer graphitic structure stacking [18, 45, 46]. Compared with those of the Pt/bulk g-C₃N₄, the (100) diffraction peaks at 12.5° of the Pt/chemically oxidized g-C₃N₄ were less intense. This was likely due to Pt clusters filling the in-plane cavities of g-C₃N₄ [20] and the partial loss of lattice nitrogen [47]. In addition, no Pt diffraction peak was observed, indicating that the Pt nanoparticles were almost homogeneously dispersed throughout the g-C₃N₄ support [20]. Notably, the gradual shift to a higher 2θ of the (002) diffraction peaks of Pt/AO and Pt/NO compared with those of their bulk counterparts corresponds to a decrease in the interplanar stacking distance. This was calculated using the Scherrer equation, as shown in Table 3.2, and it implies a strengthened interaction among the g-C₃N₄ layers. This interconnection strength can be ascribed to the substitution of more electronegative O atoms for N atoms in the framework, which will be described later.

Figure 3.8B shows the FT-IR spectra of the bulk and chemically oxidized Pt/g-C₃N₄ samples, which were used to characterize their structures. All the FT-IR spectra clearly exhibited similar peaks that can be attributed to the typical chemical bonds of pure g-C₃N₄. The strong peak at 810 cm^{-1} can be assigned to the breathing mode of triazine units [42, 48], whereas the absorption bands in the region of $1,200\text{--}1,700\text{ cm}^{-1}$ can be ascribed to the typical stretching modes of aromatic C—N and C=N in tri-s-triazine rings [42, 49]. The broad peaks in the range of $3,000\text{--}3,600\text{ cm}^{-1}$ corresponding to the N—H stretching vibrations or structural O—H groups of the Pt/AO and Pt/NO samples underwent a blue shift and a notable increase in band intensity in comparison with those of Pt/AB and Pt/NB, indicating that additional —OH functional groups were generated over the g-C₃N₄ surface after the chemical oxidation treatment [50-52]. This is later confirmed using the XPS data.

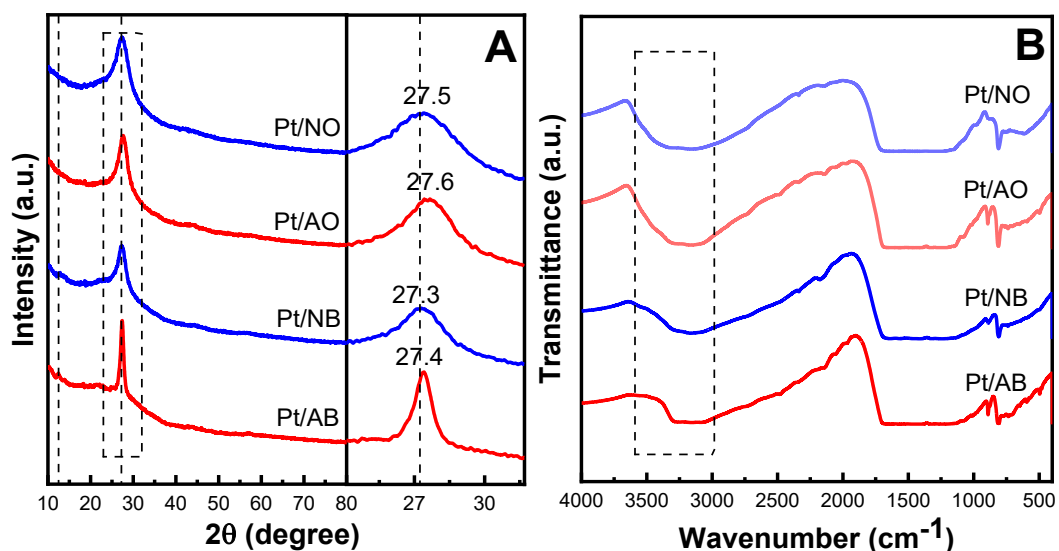


Figure 3.8. (A) XRD patterns and (B) FT-IR spectra of Pt/g-C₃N₄ photocatalysts

XPS was used to investigate the surface composition and chemical state of the as-prepared samples. As shown in Figure 3.9, the XPS survey spectra of all four samples contained sharp peaks at approximately 74, 288, 398, and 532 eV, which were assigned to Pt 4f, C 1s, N 1s, and O 1s signals, respectively [40, 53-55]. The XPS spectra of the Pt/AB, Pt/NB, Pt/AO, and Pt/NO samples are shown in Figure 3.10. For the Pt-loaded bulk g-C₃N₄ (Pt/AB and Pt/NB), the C 1s spectrum can be fitted to three peaks. The peaks with binding energies of 284.5 and 286.3 eV are derived from the C(sp²)-C(sp²) or C=C of the reference carbon on the surface and the sp³ C atoms in the carbon nitride, respectively [19, 40, 42, 56], whereas the peak at 287.5 eV is related to sp² C atoms attached to N in the aromatic rings (N-C=N) [40, 57]. Further, the C 1s spectrum of Pt/AO and Pt/NO can be deconvoluted into an additional peak at 289.2 eV, which represents the -COOH species generated during chemical oxidation [16, 17].

The existence of -COOH functional groups in Pt/AO and Pt/NO was further confirmed in the O 1s XPS spectrum by the peak at 530.6 eV [58, 59]. Compared with the O 1s spectrum of the Pt/AB and Pt/NB samples, in which there are only one main peak assigned to carbonyl (C=O) bonding at 532.4 eV [58, 60] and a small peak belonging to Pt-O at 531 eV [61, 62], there appeared another peak at 533.1 eV attributed to -OH species in the O 1s spectra of Pt/AO and Pt/NO, respectively. This is in addition to the aforementioned characteristic -COOH peak at 530.6 eV, and such peaks have been previously reported in the literature [58, 60-62]. In addition to the evidence provided by

the XPS data, the appearance of O-containing functional groups via the chemical oxidation process was further supported by an EA of O, the results of which are presented in Table 3.4. The proportions of O atoms in Pt/AO and Pt/NO (1.85 wt% and 2.52 wt%, respectively) were considerably higher than those in the Pt-loaded bulk samples (0.46 wt% in Pt/AB and 1.02 wt% in Pt/NB).

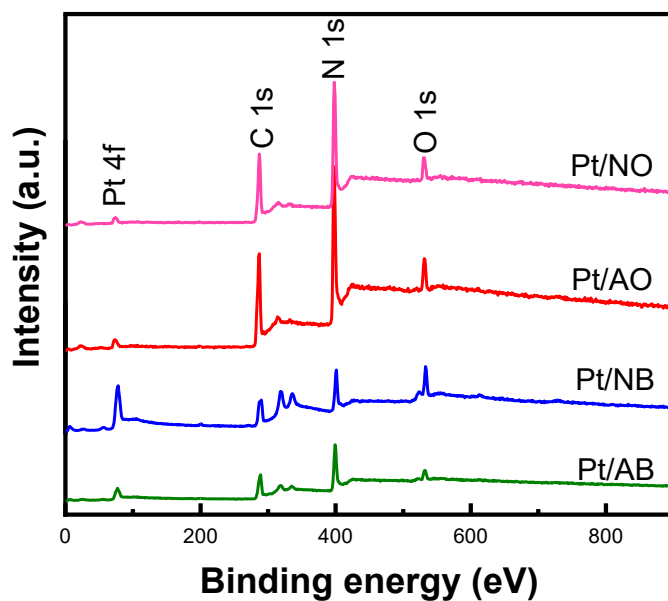


Figure 3.9. XPS survey spectra of Pt/g-C₃N₄ photocatalysts

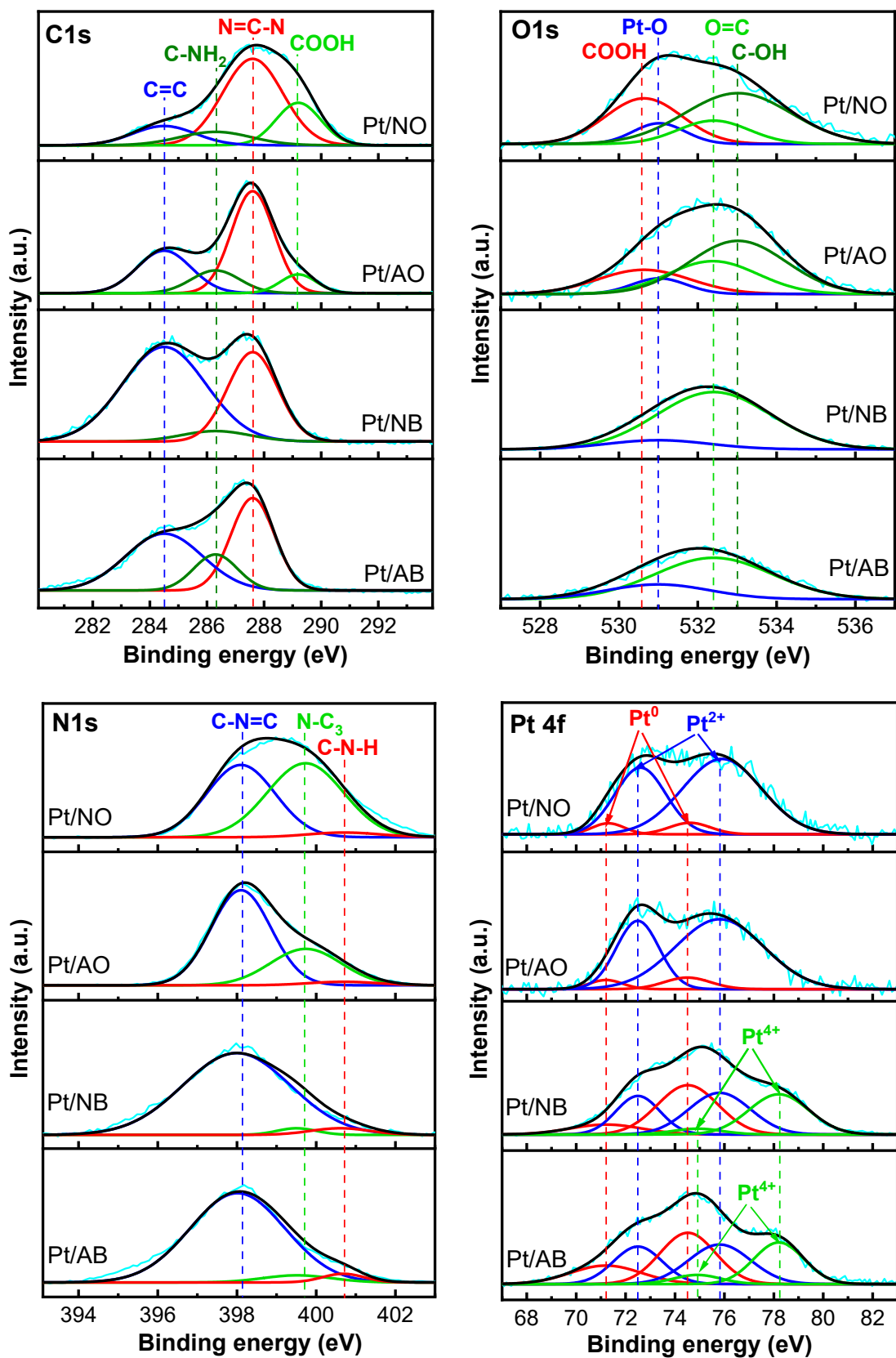


Figure 3.10. XPS spectra of C 1s, O 1s, N 1s, and Pt 4f for Pt/g-C₃N₄ photocatalysts

Table 3.4. O, H, and N contents, N-containing bond percentages, and ratios of Pt phases

Sample	wt% atom ^a			N atomic percentages (at%) ^b			Pt ²⁺ /Pt ⁰ ^c
	O	H	N	C—N=C (N _{2C})	C—NH _x	N—C ₃ (N _{3C})	
Pt/AB	0.46	1.71	59.11	90	3.8	5.3	1.03
Pt/NB	1.02	1.96	55.56	93	4.2	2.8	1.16
Pt/AO	1.85	2.87	51.78	66.8	2.9	30.3	10.8
Pt/NO	2.52	3.23	49.39	45.3	3.1	51.6	11.4

^a Oxygen, hydrogen, and nitrogen weight contents were defined using EA.

^b Different N species percentages were calculated from the N 1s XPS data.

^c Pt²⁺/Pt⁰ ratios were calculated from the deconvolution of the Pt 4f XPS data.

The N 1s spectra (Figure 3.10) reveal that there were three types of N₂ species in all four Pt/g-C₃N₄ samples. It is common knowledge that in the structure of g-C₃N₄, the N atoms in the aromatic rings are coordinated with two C atoms, whereas the trigonal N atoms that link triazine or tri-s-triazine units are coordinated with three C atoms. These three-coordinated N atoms (N_{3C}) with higher thermodynamic stability are more difficult to remove from the g-C₃N₄ structure than the two-coordinated N atoms (N_{2C}; Figure 3.11) [19, 63]. The major peak observed at 398.1 eV can be attributed to the presence of the sp²-hybridized N atom (N_{2C}) in C—N=C, and the peak related to the tertiary nitrogen N—C₃ (N_{3C} atom) is located at 399.7 eV [17, 18, 20, 42, 46, 57]. The small peak detected around 400.7 eV can be assigned to amino functional groups (C—NH_x) originating from the defective condensation of heptazine structures [40, 64]. Compared with Pt/AB and Pt/NB, the peaks assigned to C—N=C, N—C₃, and C—NH_x of Pt/AO and Pt/NO shifted to higher binding energies, which can be explained by the polarization phenomenon of electron density from the N atoms to Pt species [64, 65]. This suggests stronger metal-support interaction between Pt and g-C₃N₄ in Pt/AO and Pt/NO, which benefits the charge carriers transfer from g-C₃N₄ to Pt. Table 3.4 presents the relative amounts of different nitrogen species, calculated in units of atomic percentage (at%) on the basis of the area ratios between the respective peaks and the total area of N 1s peaks. As shown in Table 3.4, the percentages of N_{2C} atoms in Pt/AO (66.8at%) and Pt/NO (45.3at%) were much

lower than those in Pt/AB (90at%) and Pt/NB (93at%). At the same time, the figures for N_{3C} atoms were significantly higher (30.3at% and 51.6at% compared with 5.3at% and 2.8at%, respectively). These results indicate that throughout the chemical oxidation process, dicoordinated N_{2C} atoms with lower stability were detached from the $g-C_3N_4$ structure. Then, $-COOH$ and $-OH$ functional groups were generated, as evidenced by the increase in O and H atomic content and the relative decrease in the N atomic content (measured by EA) in the chemically oxidized $g-C_3N_4$ samples compared with their bulk counterparts (see Table 3.4). Further, the relative amounts of $C-NH_x$ species in Pt/AO and Pt/NO were lower than those in Pt/AB and Pt/NB, indicating that the increase in the $3,000-3,600\text{ cm}^{-1}$ FT-IR band intensity (see Figure 3.8) was due to the formation of hydroxyl groups and not amine groups.

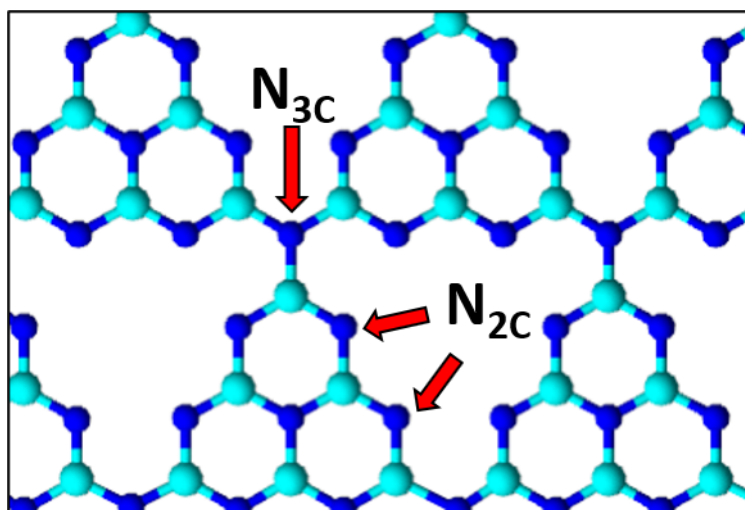


Figure 3.11. Different N species in $g-C_3N_4$ structure

Here, because more valence electrons were present in O atoms than in N atoms, the replacement of N sites by O atoms in the C–N structure would introduce extra electrons, which then delocalized into π -conjugated triazine rings [40]. The zeta potential distribution curves of the bulk and chemically oxidized $g-C_3N_4$ shown in Figure 3.12 reveal that the chemical oxidated $g-C_3N_4$ samples were more negatively charged than the bulk samples. To further investigate the change in charge structure of pristine $g-C_3N_4$ after the chemical oxidation, distributions of net atomic charges were calculated by the DFT. DFT-relaxed structures of pristine and chemically oxidized $g-C_3N_4$ systems and the

charge distribution of these two systems are shown in Figure 3.13 and Table 3.5, respectively. The Bader charge analysis [36, 37] demonstrated that the sum of atomic charges of sites 1, 2, 3, 4, 5, 6, 7, 8, 9, 10, 11, 12, 13, 14, 15, and 16 in the oxidized system (a heptazine unit after introducing O-containing functional groups) was lower than that of sites 1, 2, 3, 4, 5, 6, 7, 8, 9, 10, 11, 12, and 13 (a heptazine unit before introducing O-containing functional groups) in the pristine system, supporting experimental findings. Notably, O-containing groups such as -COOH and C=O are also known as electron-withdrawing sites, which make the remaining C–N structure of chemically oxidized g- C_3N_4 more positive. This can be supported by the lower sum of atomic charges of sites 4, 9, 10, 11, 12, and 15 in the oxidized system than that of sites 4, 6, 7, 9, 10, and 12 in the bulk system. These positively charged locales play an important role in the formation of Pt^{2+} , which will be discussed later.

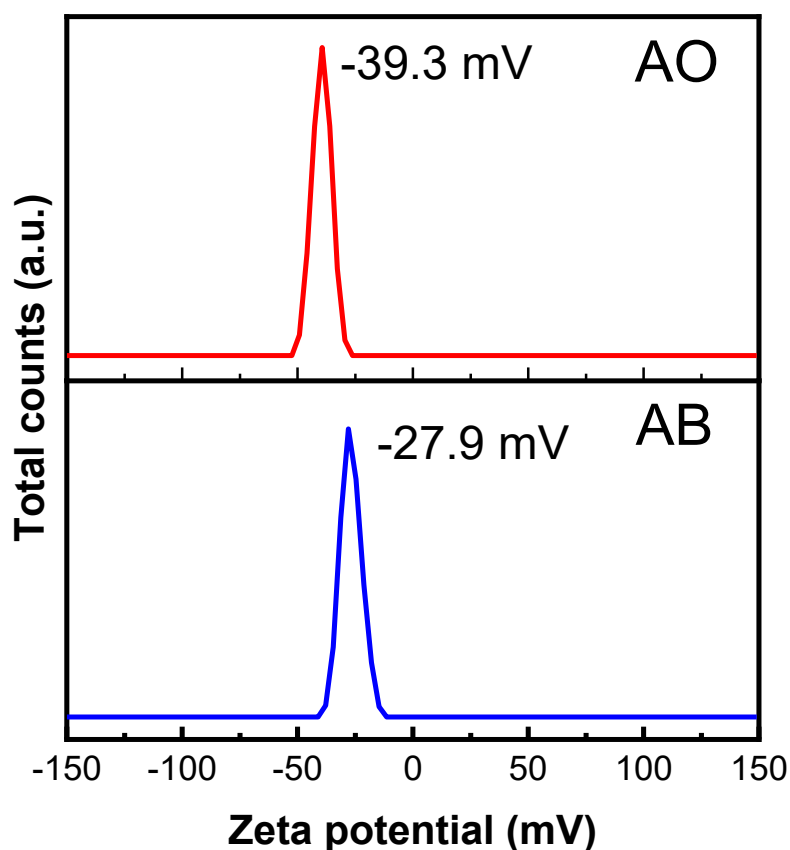


Figure 3.12. Zeta potential distribution curves of bulk and chemically oxidized g- C_3N_4

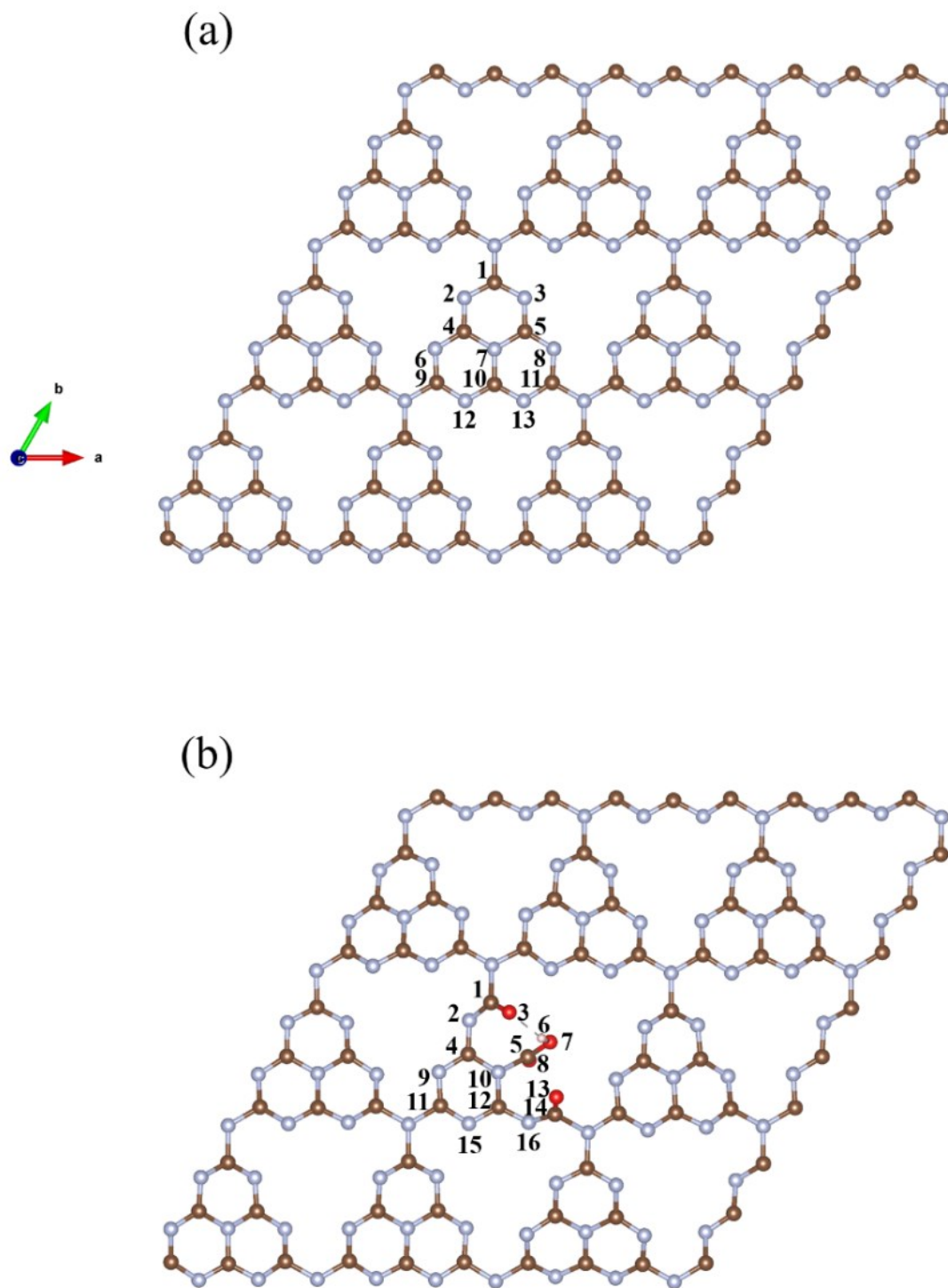


Figure 3.13. Relaxed (a) pristine and (b) chemically oxidized $g\text{-C}_3\text{N}_4$. Herein, C, N, O, and H are displayed using brown, light blue, red, and white balls, respectively

Table 3.5. Bader atomic charge (e) distribution of pristine and doped g-C₃N₄. Each number corresponds to the number in Figure 3.13

Pristine g-C ₃ N ₄ (e)		Chemically oxidized g-C ₃ N ₄ (e)	
1 (C)	1.518	1 (C)	1.722
2 (N)	-1.191	2 (N)	-1.161
3 (N)	-1.080	3 (O)	-1.114
4 (C)	1.660	4 (C)	1.510
5 (C)	1.522	5 (C)	1.876
6 (N)	-1.110	6 (H)	0.701
7 (N)	-1.371	7 (O)	-1.154
8 (N)	-1.080	8 (O)	-1.014
9 (C)	1.455	9 (N)	-1.124
10 (C)	1.660	10 (N)	-1.071
11 (C)	1.518	11 (C)	1.471
12 (N)	-1.110	12 (C)	1.561
13 (N)	-1.207	13 (O)	-1.056
		14 (C)	1.746
		15 (N)	-1.035
		16 (N)	-1.214

The chemical states of the Pt species in the Pt/g-C₃N₄ photocatalysts were examined using Pt 4f XPS spectra (see Figure 3.10). In the spectra, only two pairs of doublets were observed for chemically oxidized samples. The doublets at 71.2 and 74.5 eV can be assigned to metallic Pt species, whereas those at 72.5 and 75.8 eV can be attributed to oxidized Pt²⁺ 4f_{7/2} and Pt²⁺ 4f_{5/2}, respectively [20, 26, 66]. On the other hand, an additional pair of doublets at 74.9 and 78.2 eV corresponding to precursor Pt⁴⁺ was observed in the XPS spectra of Pt/AB and Pt/NB. The simultaneous existence of metallic Pt and oxide PtO is also observed in HR-TEM images (Figure 3.7). It is interesting to note that, in

terms of the relative contents of Pt²⁺ and Pt⁰, the chemically oxidized samples (Pt/AO and Pt/NO) witnessed an around ten-fold increase in Pt²⁺/Pt⁰ ratio compared with the bulk samples (Pt/AB and Pt/NB; see Table 3.4). Importantly, Pt²⁺ species (PtO in specific) not only demonstrate excellent efficiency in hydrogen evolution rate but also suppress the hydrogen oxidation reaction ($\text{H}_2 + \frac{1}{2} \text{O}_2 \rightarrow \text{H}_2\text{O}$). This is the undesirable back-reaction of the photocatalytic water splitting reaction, in which metallic Pt⁰ catalyzes because of its vigorous adsorption capability, low activation energy, and high adsorption energy to desorb H₂ [18, 25-27, 65]. The higher portion of Pt²⁺ in Pt/AO and Pt/NO compared with that in Pt/AB and Pt/NB is certainly one of the reasons for the witnessed enhancement in photocatalytic H₂ production described in Figure 3.2.

3.1.3 Optical properties

Generally, photocatalytic performance is greatly influenced by two factors: the number of photons absorbed by the material and the separation efficiency of the photogenerated electron–hole pairs [67]. The optical properties of the prepared samples were evaluated using UV–vis absorption spectroscopy. The UV–vis spectra of Pt/AB, Pt/NB, Pt/AO, and Pt/NO are presented in Figure 3.14A, and the calculated band gap values are shown in Table 3.2 and Figure 3.15. For all the Pt/g-C₃N₄ samples, the absorption peaks were located around 325 nm, which is in the UV range, with their shoulders tailing into the visible range. Further, a slight blue shift in the absorption peaks could be witnessed after the chemical oxidation. This corresponds to the increase in band gap energy estimated on the basis of the fitting of Tauc plots (see Table 3.2), which results from the quantum confinement effect and the addition of –OH functional groups [55, 68, 69]. However, it is clear that the chemically oxidized samples were able to absorb more photons under the same irradiating conditions due to their higher absorbance intensity [70].

The higher band gap values of Pt/AO and Pt/NO compared with those of Pt/AB and Pt/NB can also be ascribed to the blue shift in the wavelengths of their PL emission peaks (Figure 3.14B). More importantly, strong PL emission peaks emerged in the spectra of the bulk Pt/g-C₃N₄ samples, originating from the band-to-band recombination of the photoexcited electrons and holes. The fluorescence intensities of Pt/AO and Pt/NO were much lower than those of Pt/AB and Pt/NB, indicating that the chemical oxidation effectively inhibited the band-to-band recombination of the photoinduced electrons and holes [18, 40]. Time-resolved PL spectra were further investigated to obtain a quantitative

knowledge of the photogenerated charge carriers. The results are shown in Figure 3.14C, and the fitted parameters are displayed in Table 3.6. The average lifetime was calculated using the following equation:

$$\tau_{\text{ave}} = \tau_1 A_1 + \tau_2 A_2 + \tau_3 A_3,$$

where τ_1 , τ_2 , and τ_3 are the radiative lifetimes and A_1 , A_2 , and A_3 represent their relevant percentages, respectively. The remarkable prolongation of the calculated average PL lifetime values (7.74 ns for Pt/AO and 6.20 ns for Pt/NO compared with 3.48 ns for Pt/AB and 4.56 ns for Pt/NB) indicates that the charge separation efficiencies of the chemically oxidized samples were enhanced, making them advantageous for photocatalytic reactions despite their higher band gaps [6, 40, 67, 71].

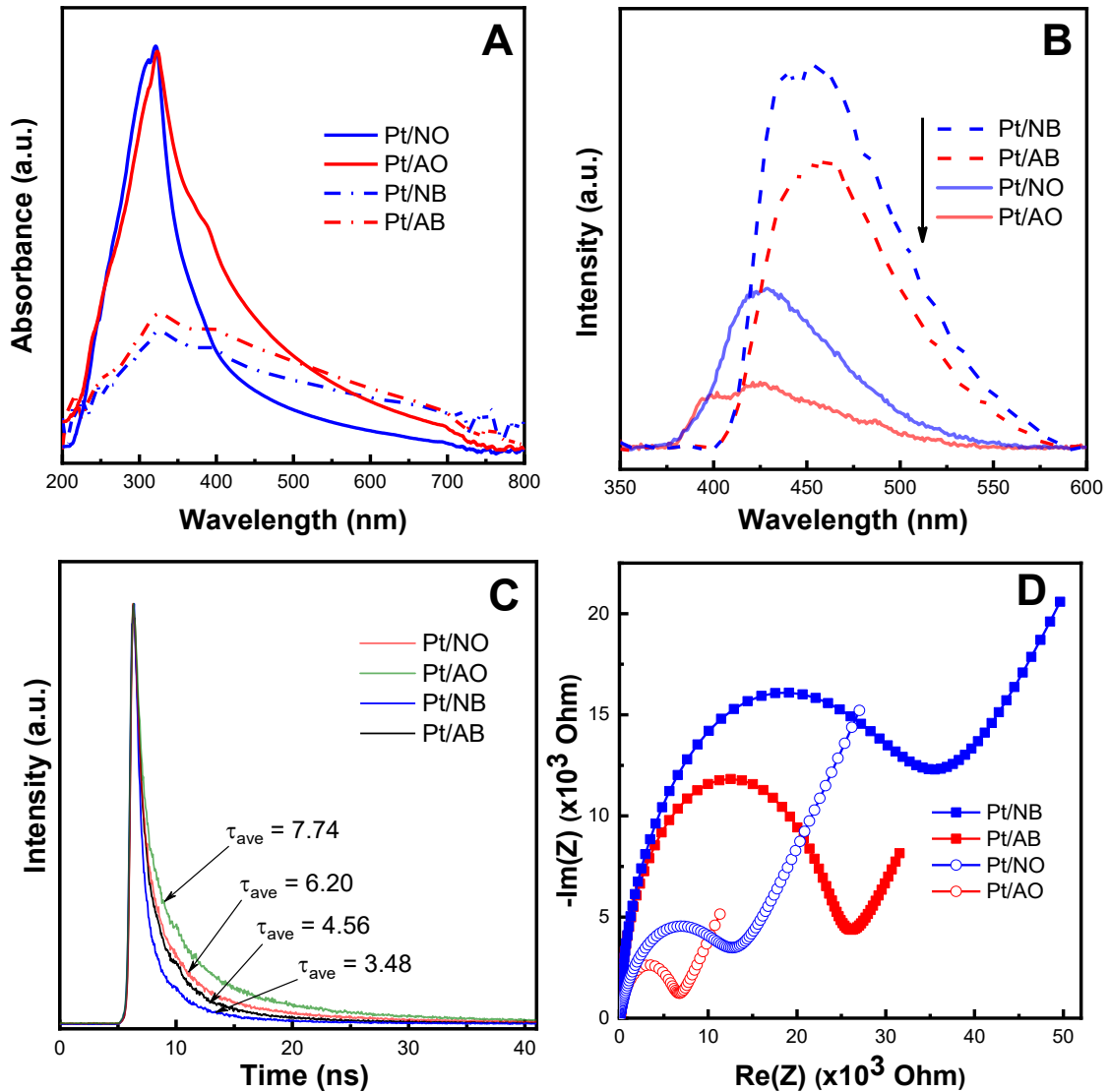


Figure 3.14. (A) UV-vis absorption spectra, (B) steady-state PL spectra, (C) time-resolved PL spectra, and (D) Nyquist plots of the Pt/g-C₃N₄ photocatalysts

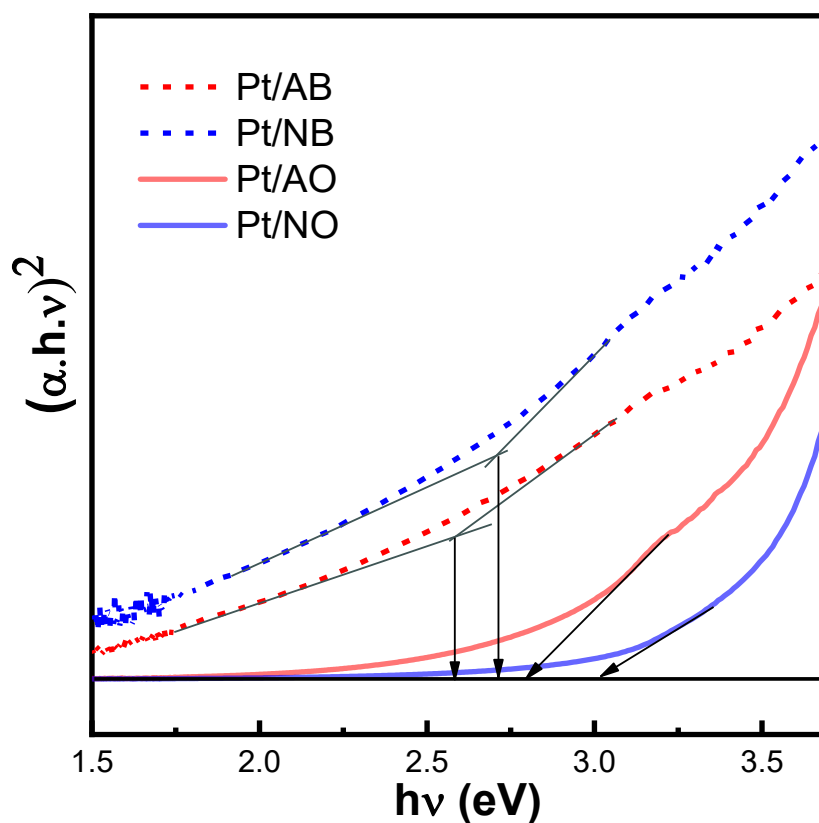


Figure 3.15. Tauc plots of Pt/g-C₃N₄ photocatalysts

Table 3.6. Fluorescence emission lifetime and relevant percentage data fitted using a three-exponential function

	τ_1 (ns)	A_1	τ_2 (ns)	A_2	τ_3 (ns)	A_3	τ_{ave} (ns)
Pt/NO	0.74	0.21	3.39	0.51	16.00	0.27	6.20
Pt/AO	0.73	0.14	3.87	0.50	15.40	0.37	7.74
Pt/NB	0.55	0.33	2.66	0.51	12.16	0.16	3.48
Pt/AB	0.65	0.22	2.90	0.58	13.69	0.20	4.56

EIS was conducted to further examine the charge transfer information and photogenerated exciton separation efficiency of the prepared photocatalysts. In general, a smaller radius in the resulting Nyquist plot reflects a more effective separation of the photoinduced electrons and holes [18, 49, 72-75]. As depicted in Figure 3.14D, the arc radii of Pt/AO and Pt/NO were significantly smaller than those of Pt/AB and Pt/NB,

indicating that the chemically oxidized Pt/g-C₃N₄ samples possessed higher charge transfer efficiency. This improvement can be attributed to: (i) the aforementioned introduction of O-containing functional groups (–COOH and –OH), which have been shown to store negative charges and increase the space charge region thickness, thus leading to improvements in upward band bending and obviously enhanced charge separation [67, 76-78] and (ii) the presence of the larger work function of Pt²⁺ as an electron-deficient species in Pt/AO and Pt/NO, which can easily trap the photoexcited electrons from g-C₃N₄ thanks to the strong metal-support interaction through the metal-semiconductor interface [26, 79]. Based on the aforementioned discussion, we can confirm that the chemical oxidation process helped to accelerate the charge separation of photoinduced electrons and holes while inhibiting the recombination rate of these charge carriers, all of which benefit the formation of oxidized Pt²⁺ phase, expediting the photocatalytic H₂ production.

3.1.4 Origin of photocatalytic activity enhancement

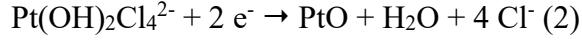
On the basis of the photocatalytic activity tests, and physicochemical and optical property characterizations, the nature of the *in situ* photodeposition of Pt on g-C₃N₄ supports in this study is described in Figure 3.3. Furthermore, the mechanism of the photocatalytic H₂ evolution process occurring on the chemically oxidized Pt/g-C₃N₄ is proposed in Figure 3.15.

The photodeposition of Pt includes three important processes (Figure 3.3). Firstly, precursor PtCl₆²⁻ undergoes hydrolysis in weakly acidic to neutral solution (measured solution pH in the photodeposition process was 4.98) following the reaction [80, 81]:



The second step is the adsorption of Pt(OH)₂Cl₄²⁻ on g-C₃N₄ support and the final is photoreduction occurring on g-C₃N₄. Under irradiation, semiconductor g-C₃N₄ absorbs the photon energy fitted to its bandgap to generate photoexcited electron–hole pairs. These photoexcited electrons then act as reduction agents of the Pt(OH)₂Cl₄²⁻ anions approaching the g-C₃N₄ surface. On the chemically oxidized g-C₃N₄, O-containing groups such as –COOH and C=O withdraw electrons, thus (i) make the remaining C–N structure becomes more positive and generate positively charged locales, hence accelerates the migration of the Pt(OH)₂Cl₄²⁻ anions onto positive sites of oxidized g-C₃N₄, and (ii) decrease the number of available reduction agents for surface-adsorbed

Pt⁴⁺. The fast Pt-precursor migration rate and its lack of reduction electrons prevent the total reduction of Pt⁴⁺ [82], and as a result, a more partially oxidized Pt²⁺ phase is formed in chemically oxidized Pt/g-C₃N₄ than in bulk g-C₃N₄ (evidenced by XPS and HR-TEM data) following the suggested reaction [83]:

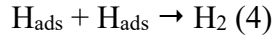


Therefore, although a similar amount of deposited Pt was measured using ICP for all four samples (see Table 3.2), the Pt²⁺/Pt⁰ ratios in the chemically oxidized samples were considerably higher.

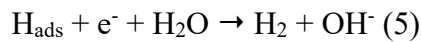
Photocatalytic H₂ evolution reaction mechanism over the chemically oxidized Pt/g-C₃N₄ photocatalysts is demonstrated in Figure 3.16. As 10 vol% TEOA was used as the sacrificial agent, the measured solution pH during the photoreaction was 10.68. Therefore, the H₂ evolution reaction follows the alkaline mechanism [25, 84], which proceeds with the formation of adsorbed hydrogen intermediates (H_{ads}) through the reduction of adsorbed water molecules on Pt²⁺ sites (Volmer step):



Subsequently, H_{ads} combine to generate H₂ and desorb from the surface of active sites PtO (Tafel step):



or react with H₂O on the same PtO atom to release H₂ molecules (Heyrovsky step):



Because of its impressive charge separation efficiency, under solar-simulated irradiation chemically oxidized g-C₃N₄ can provide an abundance of photoexcited electrons for Pt²⁺ species, which are not only the fundamental active sites of the H₂O reduction reaction but can also suppress the reversed H₂ oxidation reaction [18, 25-27, 65, 85]. Moreover, Shi's group has recently reported that the optimal oxidation state Pt²⁺ is energetically favorable for the adsorption of electron-rich H₂O and the desorption of H_{ads} [84]. Meanwhile, the photoinduced holes are consumed by the sacrificial agent TEOA through the oxidation reaction [86]. All these merits lead to the high activity of chemically oxidized Pt/g-C₃N₄ as a photocatalyst for the photocatalytic H₂ evolution reaction.

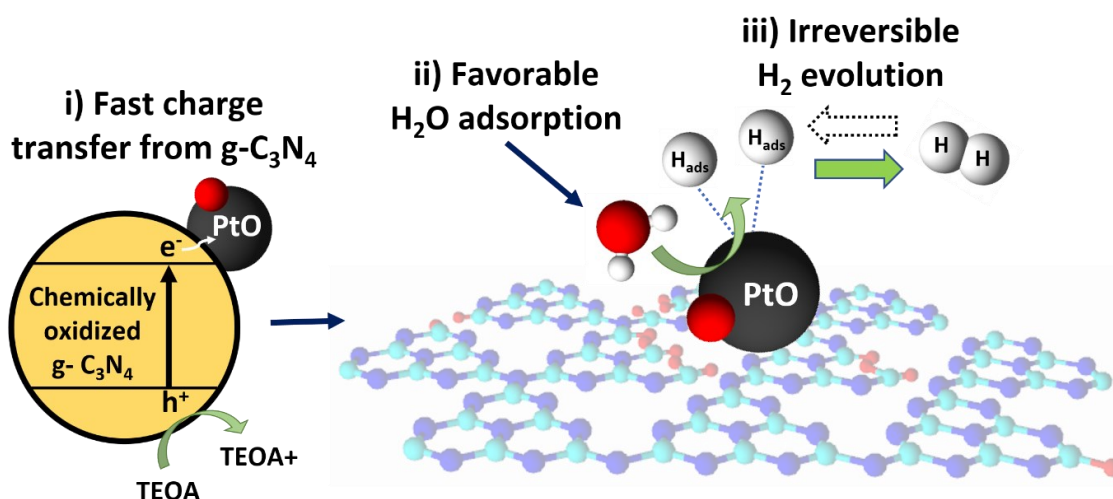


Figure 3.16. Illustration of photocatalytic H₂ evolution reaction over chemically oxidized Pt/g-C₃N₄

3.2 Different Pt-loaded g-C₃N₄ photocatalysts

3.2.1 Photocatalytic performance evaluation

Photocatalytic H₂ production based on the water splitting process of as-prepared Pt/g-C₃N₄ photocatalysts was performed in a 100-mL solution containing 10 vol.% TEOA as a hole sacrificial agent under a visible-IR irradiation system.

As shown in Figure 3.17A, after the first 6 h of irradiation, Pt/HCN exhibited outstanding H₂ production amounts (6,916.5 μmol g⁻¹) when compared with Pt/PCN (3,502.1 μmol g⁻¹) and Pt/CCN (2,459.5 μmol g⁻¹). Additionally, there was no significant drop in three 6-h cycles performances, demonstrating that all three chemically oxidized Pt/g-C₃N₄ photocatalysts are stable to photo-corrosion. The calculated average H₂ production rates in Figure 3.17B show that different Pt-loading methods could vary the H₂ production mass activity of Pt/g-C₃N₄ by 2.8 times (from 409.9 for chemical reduction method to 1,152.8 μmol g⁻¹ h⁻¹ for hydrogen reduction method) and 2.0 times (from 583.7 μmol g⁻¹ h⁻¹ for photodeposition method to 1,152.8 μmol g⁻¹ h⁻¹ for hydrogen reduction method). These results can be explained by the corresponding Pt²⁺/Pt⁰ contents in Figure 3.17B, which are consistent with the phenomenon witnessed in Chapter 3.1.

Furthermore, turnover frequencies (TOFs) of Pt/g-C₃N₄ photocatalysts, defined as H₂ production per mole of Pt loaded per hour, were calculated following the literature

[64, 65, 87]. The TOF of Pt/CCN, Pt/HCN, and Pt/PCN were found to be 70.8 h^{-1} , 187.6 h^{-1} , and 98.2 h^{-1} , respectively, which are all higher than many previously reported Pt/g-C₃N₄ catalyst systems [88-92]. These results suggest chemically oxidized g-C₃N₄ promising support for noble co-catalyst Pt by currently various loading methods.

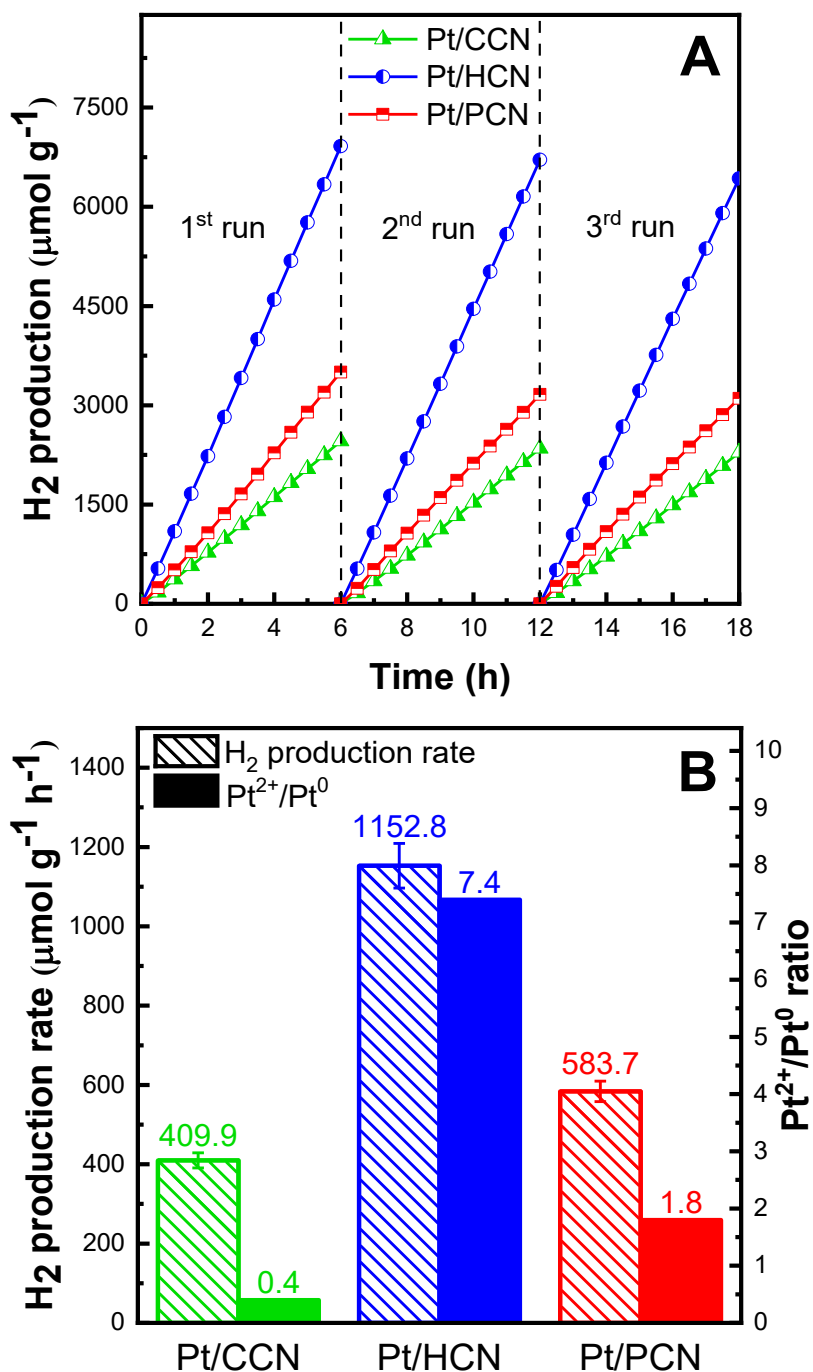


Figure 3.17. (A) Cyclic photocatalytic H₂ production over time and (B) H₂ production rates and corresponding Pt²⁺/Pt⁰ ratios of Pt/CCN, Pt/HCN, and Pt/PCN photocatalysts

3.2.2 Morphological, physicochemical, and electrical properties

Based on ICP-OES measurements, the Pt contents in Pt/CCN, Pt/HCN, and Pt/PCN were found to be 2.29%, 2.43%, and 2.35% respectively (Table 3.7), representing quite similar amounts. The textural properties of the prepared catalysts (specific surface area (S_{BET})) are also presented in Table 3.7. The chemically oxidized Pt/g- C_3N_4 sample prepared by H_2 reduction exhibited higher S_{BET} and similar average pore size compared with the Pt/g- C_3N_4 samples prepared by chemical reduction and photoreduction. The corresponding N_2 adsorption–desorption isotherms of the Pt/g- C_3N_4 materials are shown in Figure 3.18. According to Brunauer–Deming–Deming–Teller classification, all of the samples exhibited type-IV isotherms with an H3 hysteresis loop, implying that the prepared materials were mesoporous solids possessing nanosheet structures [19, 20].

Table 3.7. Physicochemical and optical properties of Pt/g- C_3N_4 photocatalysts

Sample	Pt content (wt.%)^a	S_{BET} ($\text{m}^2 \text{g}^{-1}$)^b	Pt average size (nm)^c	Band gap (eV)^d
Pt/CCN	2.29	43.56	100	2.94
Pt/HCN	2.43	53.96	1-2	3.02
Pt/PCN	2.35	46.94	6	2.88

^a Platinum contents were defined using ICP-OES.

^b Specific surface area (S_{BET}) was determined via N_2 adsorption–desorption isotherm measurements.

^c Estimated average platinum particle sizes were obtained from TEM and AFM images.

^d Estimated band gaps were obtained from UV–Vis spectra.

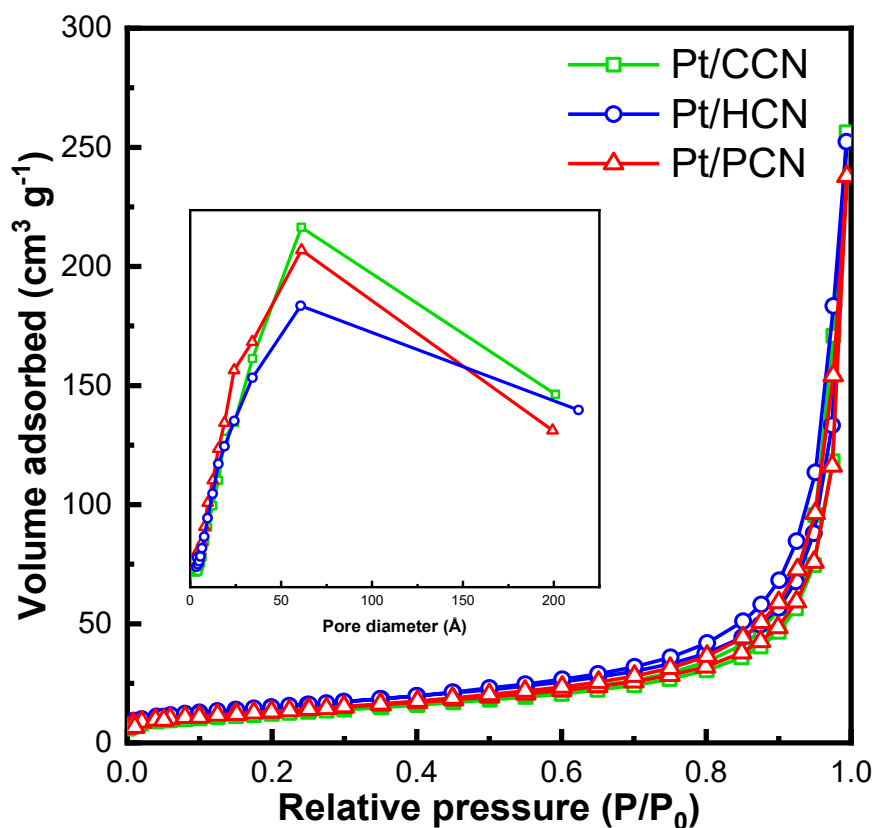


Figure 3.18. Nitrogen adsorption–desorption isotherms (inset: pore diameter distribution) of Pt/g-C₃N₄ photocatalysts

The surface morphologies of the Pt/CCN, Pt/HCN, and Pt/PCN samples were characterized using SEM and FE-TEM, and the results are shown in Figures 3.19 and Figure 3.20, respectively. SEM images of Pt/CCN in Figure 3.19 show that Pt particles are observable as bright dots, indicating their large particle size. This is further confirmed by FE-TEM images of Pt/CCN (Figure 3.20A), where Pt clusters are seen to be agglomerated to a size of about 100 nm. For Pt/PCN (Figure 3.20D), Pt particles are better distributed, with an average size of about 6 nm. Besides, in the high-magnification images in Figure 3.20B and 3.20E, lattice fringes characteristic of Pt⁰ (0.23 nm) and PtO (0.27 nm) can be observed in both Pt/CCN and Pt/PCN, proving the coexistence of Pt and PtO species in these samples [44]. No Pt particles can be observed on the surface of the Pt/HCN sample in Figure 3.20C. However, the existence of Pt on g-C₃N₄ surface in Pt/HCN can be witnessed as white dots in EDS mapping of Pt in Figure 3.21B and AFM image in Figure 3.22A, with a high distribution of Pt all over the g-C₃N₄ surface. Besides, AFM cross-sectional profile (Figure 3.22B) reveals the heights of Pt particles are in the range of 0.5 to 1 nm.

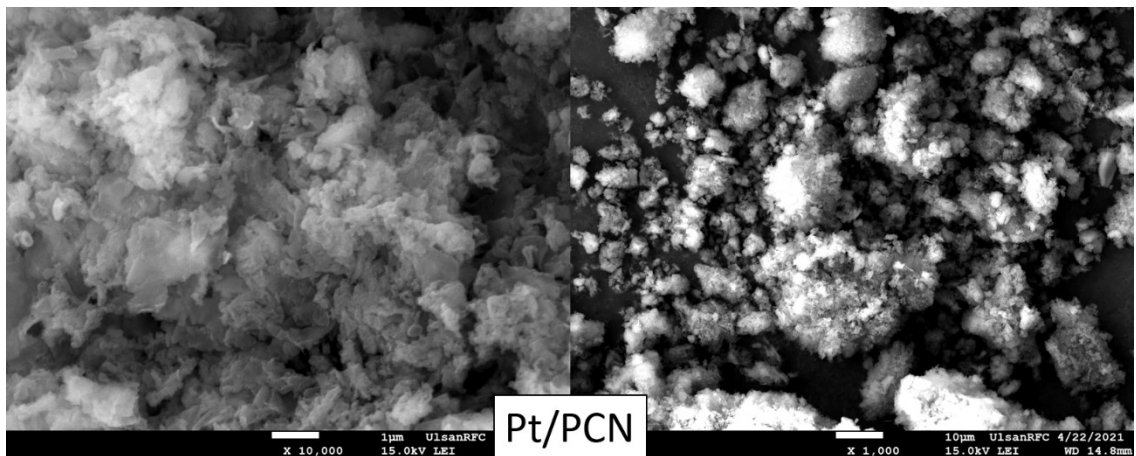
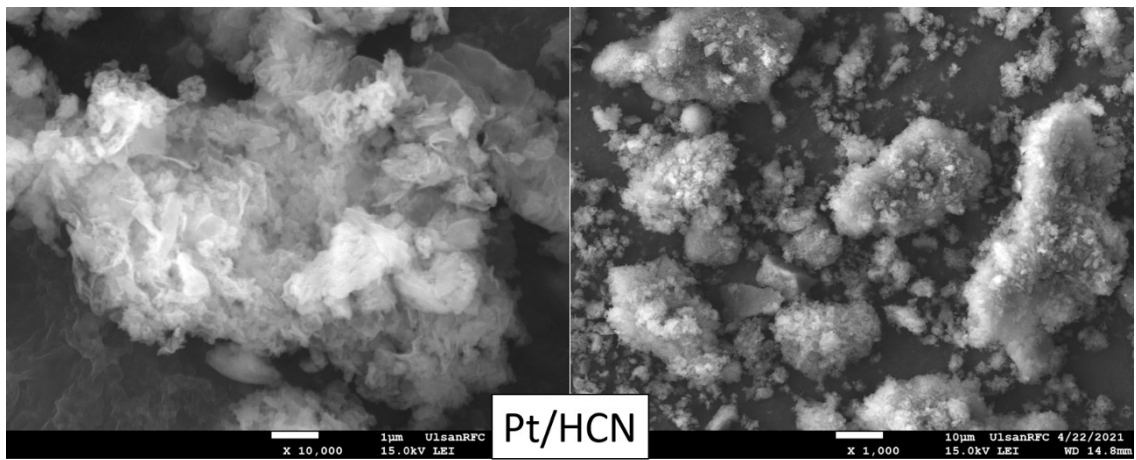
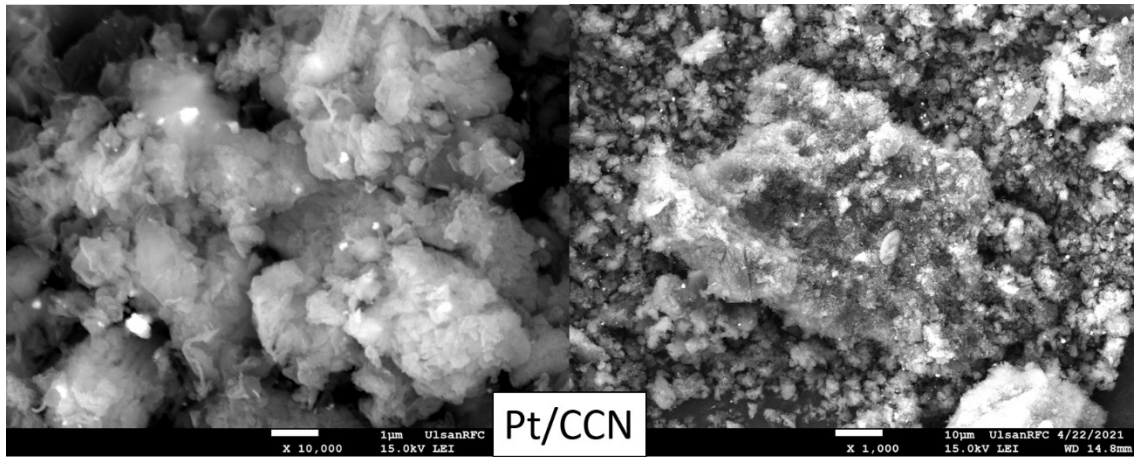


Figure 3.19. FE-SEM images of Pt/g-C₃N₄ photocatalysts

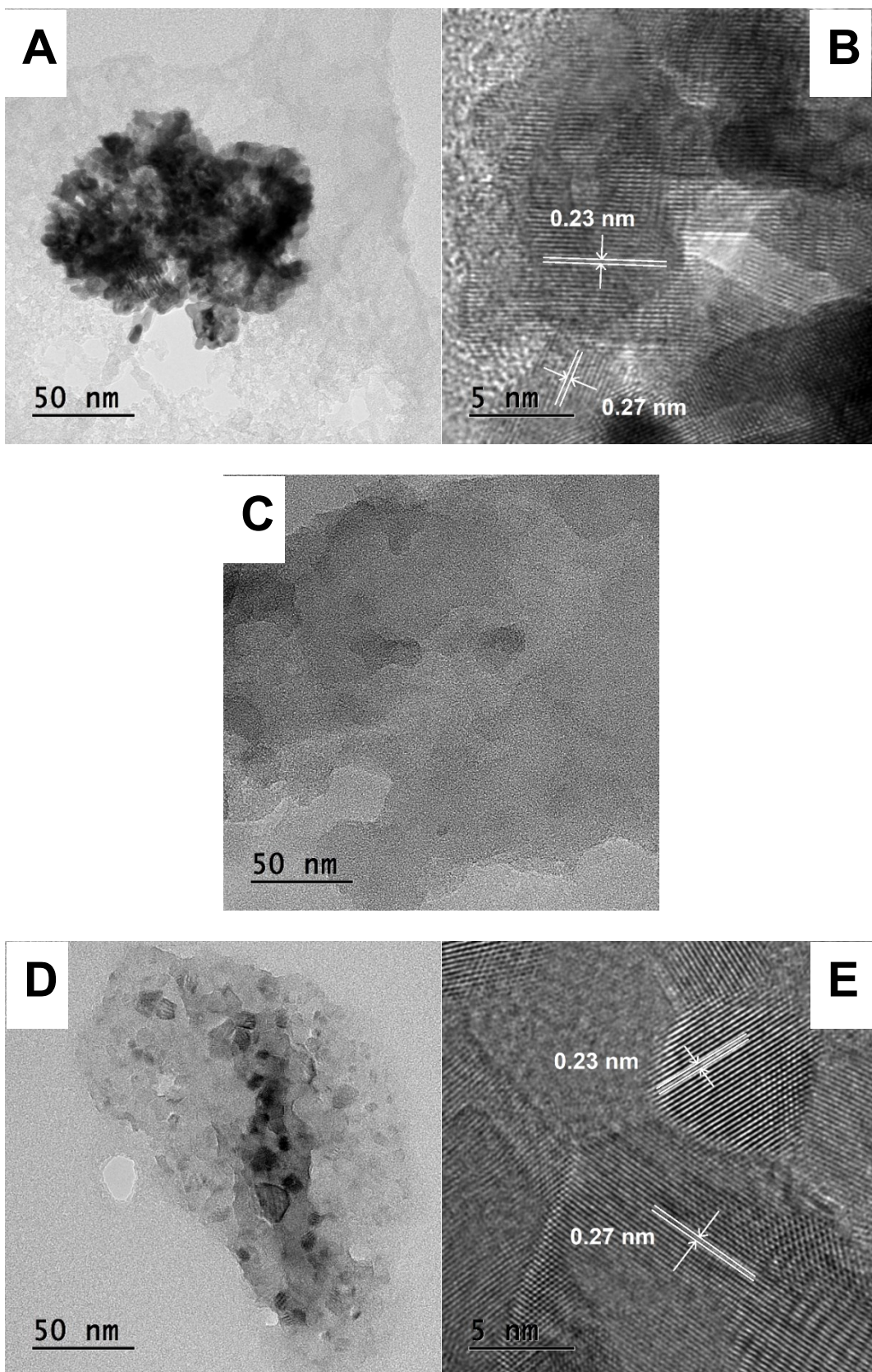


Figure 3.20. FE-TEM images of (A and B) Pt/CCN, (C) Pt/HCN, and (D and E) Pt/PCN.

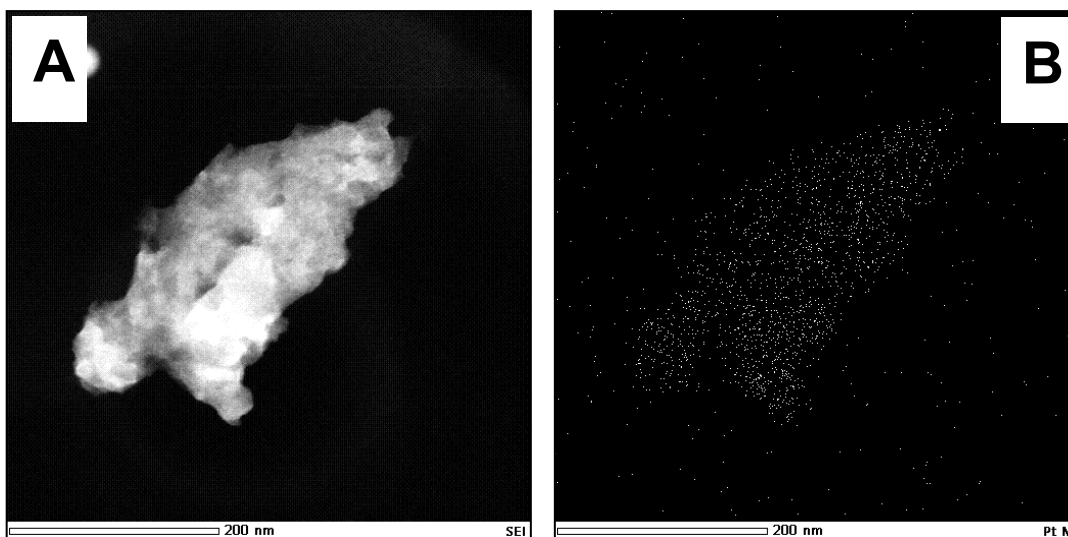


Figure 3.21. (A) STEM image and (B) corresponding Pt EDS mapping of Pt/HCN

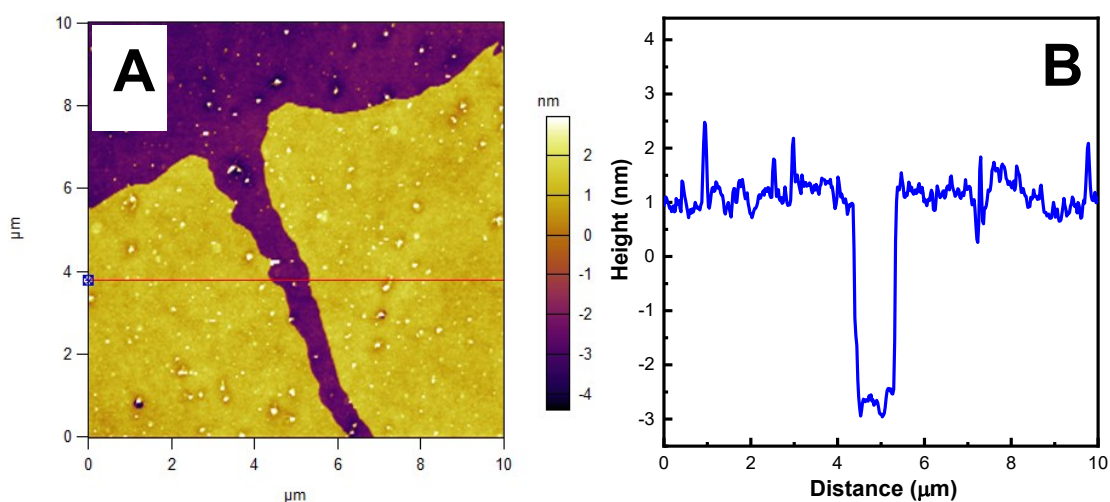


Figure 3.22. (A) AFM image and (B) corresponding cross-sectional profile of Pt/HCN

Figure 3.23A displays the XRD spectra of the chemically oxidized Pt/g-C₃N₄ samples. In all the samples, there was a main characteristic peak at $2\theta = 27.5^\circ$, corresponding to the (002) plane of pure g-C₃N₄, which can be ascribed to interlayer graphitic structure stacking [18, 45, 46]. This reveals that the g-C₃N₄ structures are maintained throughout any of the three reduction methods. In addition, a series of peaks appeared at 37.8° , 46.3° , 67.9° , and 81.4° are characteristic peaks of the cubic Pt structure [44]. However, no Pt diffraction peak was observed in Pt/HCN and Pt/PCN, indicating that the Pt nanoparticles were almost homogeneously dispersed throughout the g-C₃N₄

support, while the poor dispersion of Pt led to larger sized Pt anchoring on Pt/CCN surface [20, 86].

Figure 3.23B shows the FT-IR spectra of the chemically oxidized Pt/g-C₃N₄ samples, which were used to characterize their structures. All the FT-IR spectra clearly exhibited similar peaks that can be attributed to the typical chemical bonds of pure g-C₃N₄. The strong peak at 810 cm⁻¹ can be assigned to the breathing mode of triazine units [42, 48], whereas the absorption bands in the region of 1,200–1,700 cm⁻¹ can be ascribed to the typical stretching modes of aromatic C–N and C=N in tri-s-triazine rings [42, 49]. The broad peaks in the range of 3,000–3,600 cm⁻¹ correspond to the N–H stretching vibrations or structural O–H groups of the Pt/g-C₃N₄ samples. The intensity of these peaks is higher in Pt/CCN due to the addition of NHNH₂ groups during the hydrazinolysis (see Figure 3.24) [93].

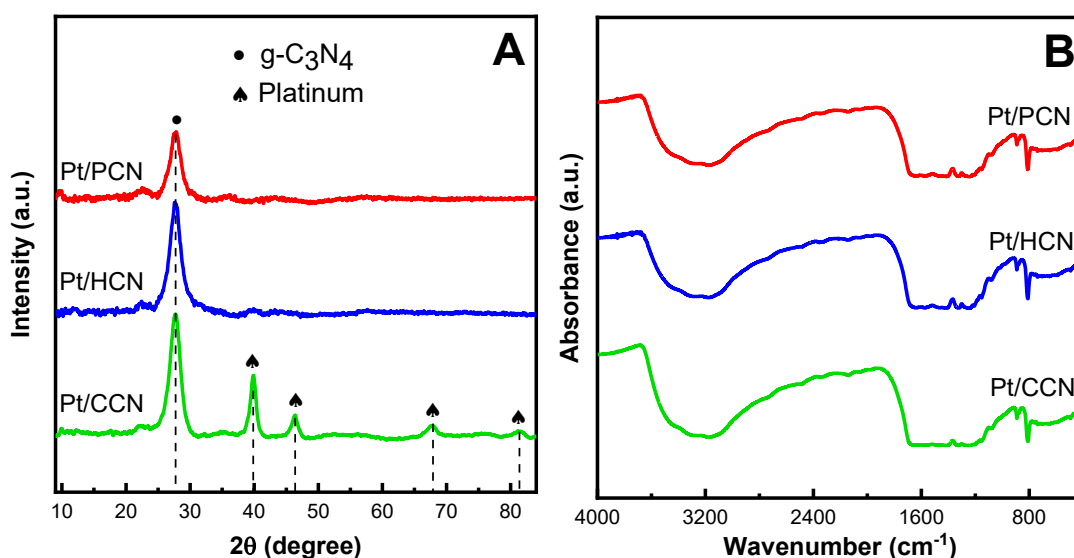


Figure 3.23. (A) XRD patterns and (B) FT-IR spectra of Pt/g-C₃N₄ photocatalysts

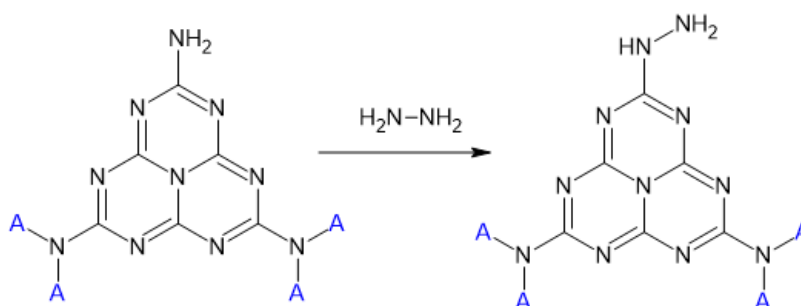


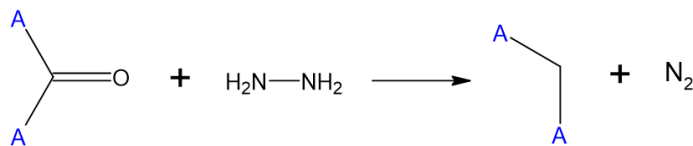
Figure 3.24. Hydrazinolysis of g-C₃N₄

XPS was used to investigate the surface composition and chemical state of the as-prepared samples. As shown in Figure 3.25, the XPS survey spectra of all four samples contained sharp peaks at approximately 74, 288, 398, and 532 eV, which were assigned to Pt 4f, C 1s, N 1s, and O 1s signals, respectively [40, 53-55]. The XPS spectra of the Pt/CCN, Pt/HCN, and Pt/PCN, samples are shown in Figure 3.26. For all the samples, the C 1s spectrum can be fitted to four peaks. The peaks with binding energies of 284.6 and 286.5 eV are derived from the C(sp²)-C(sp²) or C=C of the reference carbon on the surface and the sp³ C atoms in the carbon nitride, respectively [19, 40, 42, 56], whereas the peak at 287.5 eV is related to sp² C atoms attached to N in the aromatic rings (N-C=N) [40, 57]. The C 1s spectrum can also be deconvoluted into a small peak at 289.0 eV, which represents the -COOH species generated during chemical oxidation [16, 17].

The N 1s spectra (Figure 3.26) reveal that there were three types of nitrogen species in all four Pt/g-C₃N₄ samples. The major peak observed at 397.8 eV can be attributed to the presence of the sp²-hybridized N atom in C-N=C, and the peak related to the tertiary nitrogen N-C₃ is located at 399.2 eV [17, 18, 20, 42, 46, 57]. The small peak detected around 400.1 eV can be assigned to amino functional groups (C-NH_x) originating from the defective condensation of heptazine structures [40, 64].

The existence of -COOH functional groups in chemically oxidized g-C₃N₄ (CN) and Pt/g-C₃N₄ was further confirmed in the O 1s XPS spectrum by the peak at 530.8 eV [58, 59]. In the O 1s spectrum of the Pt/g-C₃N₄ samples, besides the aforementioned characteristic -COOH peak at 530.4 eV, a peak assigned to carbonyl (C=O) bonding at 531.6 eV [58, 60], and a peak at 533.1 eV attributed to -OH species [17], there appeared another peak at 531.0 eV of Pt-O species. Table 3.8 presents the O/C atomic ratios and relative amounts of different oxygen species, calculated in units of atomic percentage (at%) based on the area ratios between the respective peaks and the total area of O 1s peaks. As shown in Table 3.8, after loading Pt the O/C atomic ratios of all three samples decrease compared with CN, implying that O atoms were exploited through the reduction of Pt precursor. This ratio is the lowest for Pt/CCN (0.10), which can be explained by the highest reduction ability of hydrazine. The component ratios of oxygen species in Pt/PCN are quite similar to CN, except for the appearance of Pt-O. The percentages of -COOH and -OH species in Pt/HCN (13.6 and 10 at%, respectively) were much lower than those before loading Pt (28.8 and 17.1 at%, respective). This can be explained by the reaction

of H^* radicals disassociated from H_2 catalyzed by platinum with surface $-OH$ groups on CN in the H_2 reduction step [94]. The significant lower percentages of $-COOH$ and $C=O$ species in Pt/CCN after loading Pt (21 and 32.5 at% comparing to 28.8 and 54.1 at%, respectively) can be ascribed to the reaction of carbonyl groups with hydrazine [95, 96]:



The chemical states of the Pt species in the Pt/g- C_3N_4 photocatalysts were examined using Pt 4f XPS spectra (see Figure 3.26). In the spectra, three pairs of doublets were observed for Pt/HCN and Pt/PCN, while only two were seen for Pt/CCN. The doublets at 71.2 and 74.5 eV can be assigned to metallic Pt species, whereas those at 72.4 and 75.8 eV can be attributed to oxidized Pt^{2+} 4f_{7/2} and Pt^{2+} 4f_{5/2}. For Pt/HCN and Pt/PCN, those at 76.5 and 77.9 eV can be assigned to Pt^{4+} 4f_{7/2} and Pt^{4+} 4f_{5/2}, respectively [20, 26, 66]. It is interesting to note that, in terms of the relative contents of Pt^{2+} , the sample prepared by H_2 reduction (Pt/HCN) witnessed a more than eight-teen-fold and four-fold increase in Pt^{2+}/Pt^0 ratio compared with that prepared by chemical reduction and photoreduction, respectively (see Table 3.9).

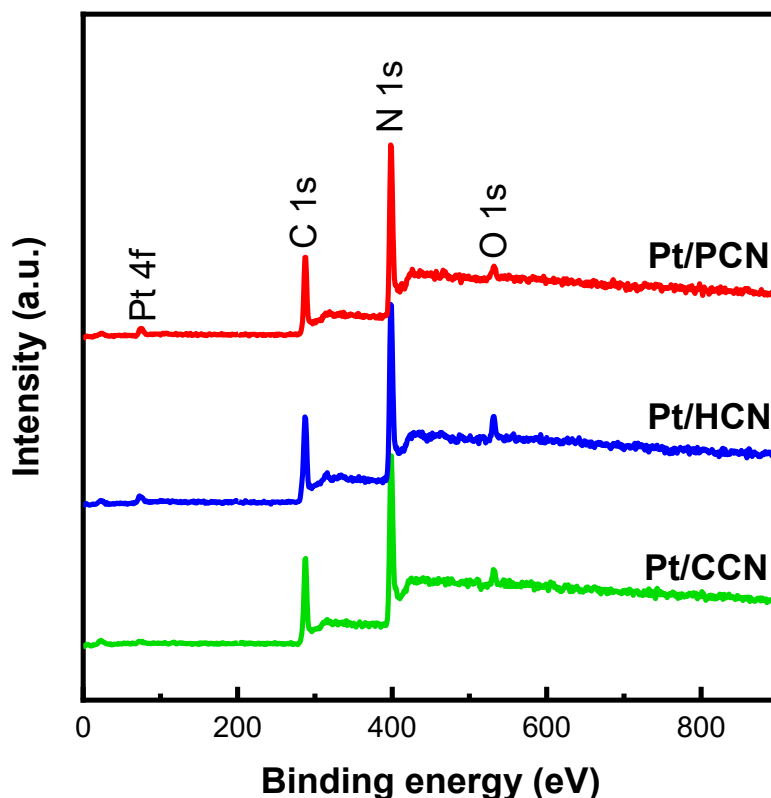


Figure 3.25. XPS survey spectra of Pt/g- C_3N_4 photocatalysts

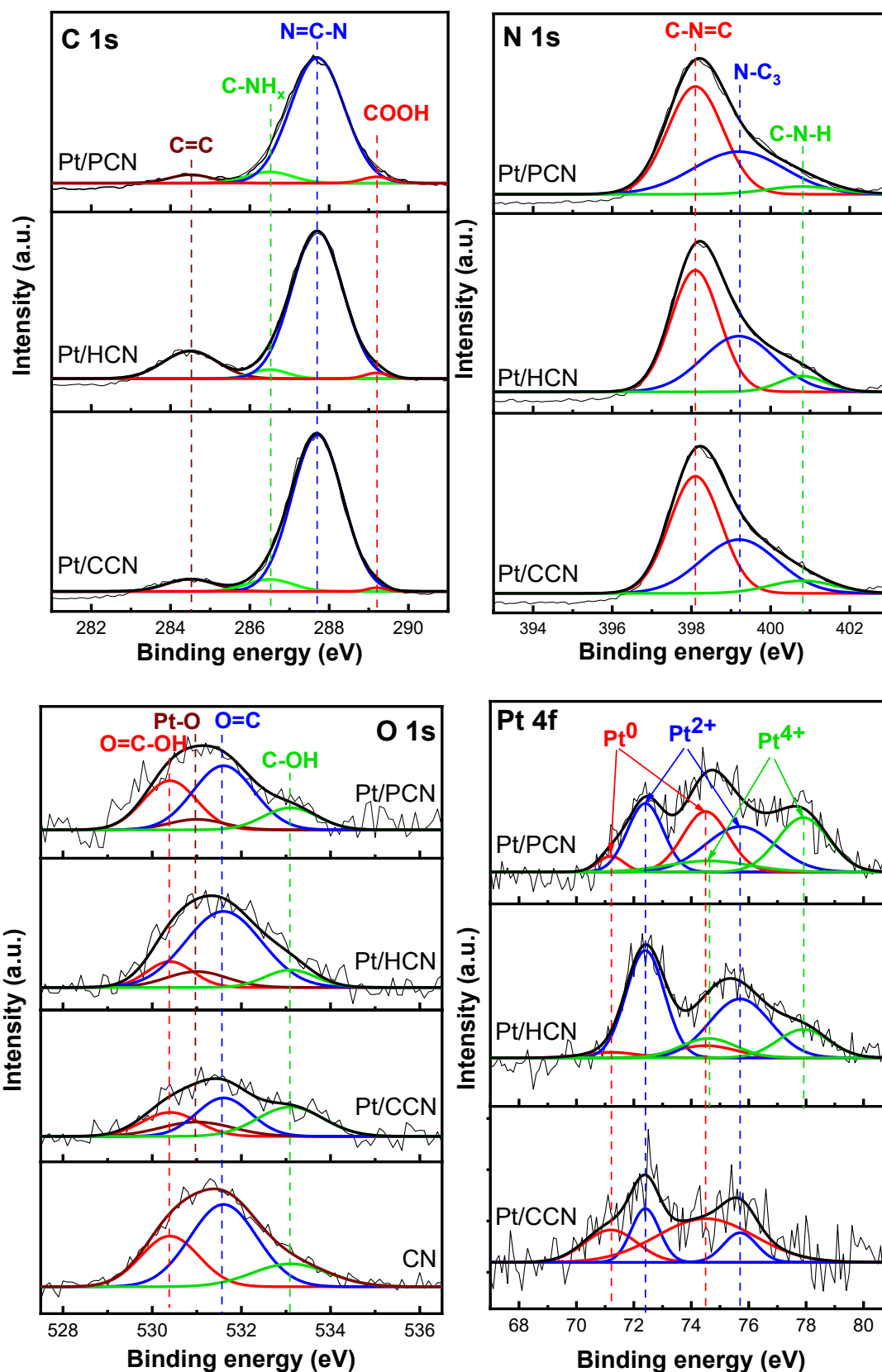


Figure 3.26. XPS spectra of C 1s, N 1s, O 1s, and Pt 4f for Pt/g-C₃N₄ photocatalysts

Table 3.8. O 1s XPS analysis results

Samples	Atomic ratio	% atoms			
	O/C	—COOH	Pt—O	O=C	C—OH
Pt/PCN	0.13	31.5	7.0	47.1	14.4
Pt/HCN	0.13	13.6	10.9	65.5	10.0
Pt/CCN	0.10	21.0	16.1	32.5	30.3
CN	0.17	28.8	-	54.1	17.1

^a Different O species percentages were calculated from the O 1s XPS data.

Table 3.9. Pt species and corresponding H₂ production rates of Pt/g-C₃N₄ photocatalysts

Sample	Pt-loading method	Pt ⁰ (at%) ^a	Pt ²⁺ (at%) ^a	Pt ⁴⁺ (at%) ^a	Pt ²⁺ /Pt ⁰	H ₂ (μmol g ⁻¹ h ⁻¹)
Pt/CCN	Chemical reduction	70.4	29.6	0	0.4	409.9
Pt/HCN	H ₂ reduction	9.2	68.5	22.3	7.4	1,152.8
Pt/PCN	Photoreduction	25.3	45.0	29.6	1.8	583.7

^a Different Pt species percentages were calculated from the deconvolution of the Pt 4f XPS data.

3.2.3 Optical properties

Generally, photocatalytic performance is greatly influenced by two factors: the number of photons absorbed by the material and the separation efficiency of the photogenerated electron–hole pairs [67]. The optical properties of the prepared samples were evaluated using UV–vis absorption spectroscopy. The UV–vis spectra of Pt/CCN, Pt/HCN, and Pt/PCN are presented in Figure 3.27A, and the calculated band gap values are shown in Table 3.7 and Figure 3.27B. For all the Pt/g-C₃N₄ samples, the absorption peaks were located around 335 nm, which is in the UV range, with their shoulders tailing into the visible range.

Photoluminescence spectra in Figure 3.27C shows quite similar PL intensities and peak positions at about 420 nm of the three samples, which is in the visible range. Time-resolved PL spectra were further investigated to obtain a quantitative knowledge of the photogenerated charge carriers. The results and the fitted parameters are shown in Figure 3.27D. The average lifetime was calculated using the following equation:

$$\tau_{ave} = \tau_1 A_1 + \tau_2 A_2 + \tau_3 A_3,$$

where τ_1 , τ_2 , and τ_3 are the radiative lifetimes and A_1 , A_2 , and A_3 represent their relevant percentages, respectively. The higher calculated average PL lifetime values (3.81 ns for Pt/HCN and 3.78 ns for Pt/PCN compared with 2.94 ns for Pt/CCN) indicates that the charge separation efficiencies of the Pt/HCN sample and Pt/PCN are higher than that of Pt/CCN.

EIS was conducted to further examine the charge transfer information and photogenerated exciton separation efficiency of the prepared photocatalysts. In general, a smaller radius in the resulting Nyquist plot reflects a more effective separation of the photoinduced electrons and holes [18, 49, 72-75]. As depicted in Figure 3.27E, the arc radii of three samples follow the order: Pt/HCN < Pt/PCN < Pt/CCN, indicating that the Pt/g-C₃N₄ sample prepared by H₂ reduction possessed the highest charge transfer efficiency, while the sample prepared by chemical reduction exhibited the poorest charge migration. This result is consistent with the above PL and time-resolve PL data.

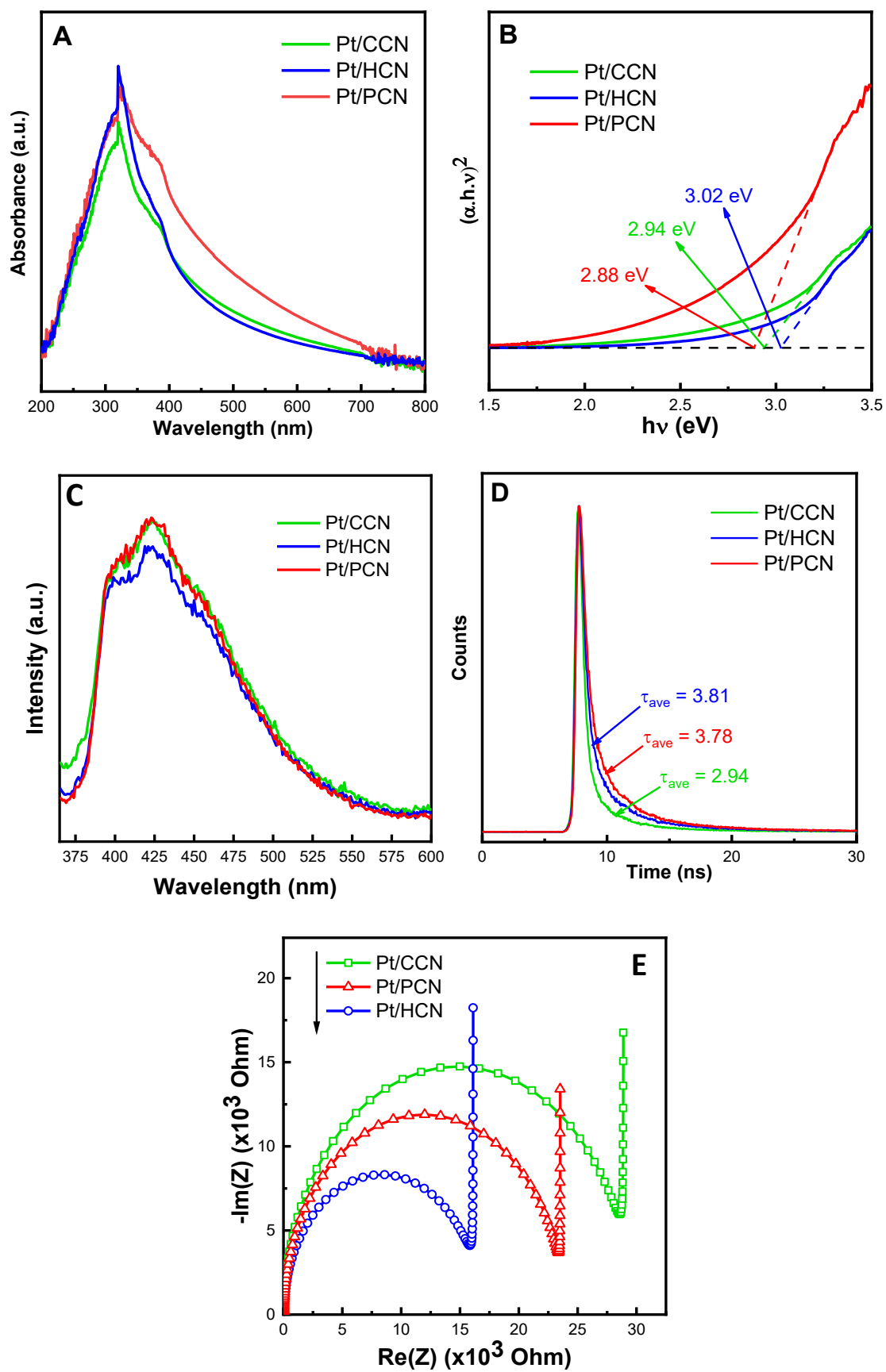


Figure 3.27. (A) UV-vis absorption spectra, (B) Tauc plots, (C) steady-state PL spectra, (D) time-resolved PL spectra, and (E) Nyquist plots of the Pt/g-C₃N₄ photocatalysts

Chapter 4: Conclusions

In this work, a simple chemical oxidation method of bulk g-C₃N₄ and the different decoration methods of Pt as a co-catalyst were employed to develop a novel Pt/g-C₃N₄ photocatalyst for the photocatalytic H₂ production reaction. The chemically oxidized g-C₃N₄ samples with O-containing functional groups were found to have a surface with several positively charged locales, thus promoting the generation of Pt²⁺ species instead of metallic Pt⁰ in the photodeposition process and improving the charge separation efficiency of the Pt/g-C₃N₄ photocatalysts. These distinct features of the chemically oxidized Pt/g-C₃N₄ ensured an excellent photocatalytic water splitting performance under solar-simulated irradiation, with the H₂ production rate reaching 3,640.8 μmol g⁻¹ h⁻¹. Among three different typical decorating methods of Pt on chemically oxidized g-C₃N₄ support, the hydrogen reduction method brings the highest Pt²⁺/Pt⁰ ratio. These distinct features of the chemically oxidized Pt/g-C₃N₄ prepared by the hydrogen reduction method ensured excellent photocatalytic water splitting performance under solar-simulated irradiation.

References

- [1] Total final energy consumption, Enerdata.
- [2] Global Greenhouse Gas Emissions Data.
- [3] J. Xing, H.B. Jiang, J.F. Chen, Y.H. Li, L. Wu, S. Yang, L.R. Zheng, H.F. Wang, P. Hu, H.J. Zhao, Active sites on hydrogen evolution photocatalyst, *Journal of Materials Chemistry A*, 1 (2013) 15258-15264.
- [4] T. Jafari, E. Moharreri, A.S. Amin, R. Miao, W. Song, S.L. Suib, Photocatalytic water splitting—the untamed dream: a review of recent advances, *Molecules*, 21 (2016) 900.
- [5] B. Lin, G. Yang, B. Yang, Y. Zhao, Construction of novel three dimensionally ordered macroporous carbon nitride for highly efficient photocatalytic activity, *Applied Catalysis B: Environmental*, 198 (2016) 276-285.
- [6] J. Wen, J. Xie, X. Chen, X. Li, A review on g-C₃N₄-based photocatalysts, *Applied surface science*, 391 (2017) 72-123.
- [7] K. Li, F.-Y. Su, W.-D. Zhang, Modification of g-C₃N₄ nanosheets by carbon quantum dots for highly efficient photocatalytic generation of hydrogen, *Applied Surface Science*, 375 (2016) 110-117.
- [8] A. Muhammad, M. Tahir, S.S. Al-Shahrani, A.M. Ali, S.U. Rather, Template free synthesis of graphitic carbon nitride nanotubes mediated by lanthanum (La/g-CNT) for selective photocatalytic CO₂ reduction via dry reforming of methane (DRM) to fuels, *Applied Surface Science*, 504 (2020) 144177.
- [9] Q. Li, Z. Sun, H. Wang, Z. Wu, Insight into the enhanced CO₂ photocatalytic reduction performance over hollow-structured Bi-decorated g-C₃N₄ nanohybrid under visible-light irradiation, *Journal of CO₂ Utilization*, 28 (2018) 126-136.
- [10] J. Yi, W. El-Alami, Y. Song, H. Li, P.M. Ajayan, H. Xu, Emerging surface strategies on graphitic carbon nitride for solar driven water splitting, *Chemical Engineering Journal*, 382 (2020) 122812.
- [11] T. Xu, D. Wang, L. Dong, H. Shen, W. Lu, W. Chen, Graphitic carbon nitride co-modified by zinc phthalocyanine and graphene quantum dots for the efficient photocatalytic degradation of refractory contaminants, *Applied Catalysis B: Environmental*, 244 (2019) 96-106.
- [12] A. Akhundi, A. Habibi-Yangjeh, M. Abitorabi, S. Rahim Pourn, Review on photocatalytic conversion of carbon dioxide to value-added compounds and renewable fuels by graphitic carbon nitride-based photocatalysts, *Catalysis Reviews*, 61 (2019) 595-628.
- [13] X. Ji, X. Yuan, J. Wu, L. Yu, H. Guo, H. Wang, H. Zhang, D. Yu, Y. Zhao, Tuning the photocatalytic activity of graphitic carbon nitride by plasma-based surface modification, *ACS applied materials & interfaces*, 9 (2017) 24616-24624.

- [14] L. Jing, R. Zhu, D.L. Phillips, J.C. Yu, Effective prevention of charge trapping in graphitic carbon nitride with nanosized red phosphorus modification for superior photo (electro) catalysis, *Advanced Functional Materials*, 27 (2017) 1703484.
- [15] L. Chen, J. Song, Tailored graphitic carbon nitride nanostructures: synthesis, modification, and sensing applications, *Advanced Functional Materials*, 27 (2017) 1702695.
- [16] H.-J. Li, B.-W. Sun, L. Sui, D.-J. Qian, M. Chen, Preparation of water-dispersible porous g-C₃N₄ with improved photocatalytic activity by chemical oxidation, *Physical Chemistry Chemical Physics*, 17 (2015) 3309-3315.
- [17] T.K.A. Nguyen, T.-T. Pham, H. Nguyen-Phu, E.W. Shin, The effect of graphitic carbon nitride precursors on the photocatalytic dye degradation of water-dispersible graphitic carbon nitride photocatalysts, *Applied Surface Science*, (2020) 148027.
- [18] M. Liu, P. Xia, L. Zhang, B. Cheng, J. Yu, Enhanced photocatalytic H₂-production activity of g-C₃N₄ nanosheets via optimal photodeposition of Pt as cocatalyst, *ACS Sustainable Chemistry & Engineering*, 6 (2018) 10472-10480.
- [19] P. Zhou, F. Lv, N. Li, Y. Zhang, Z. Mu, Y. Tang, J. Lai, Y. Chao, M. Luo, F. Lin, Strengthening reactive metal-support interaction to stabilize high-density Pt single atoms on electron-deficient g-C₃N₄ for boosting photocatalytic H₂ production, *Nano energy*, 56 (2019) 127-137.
- [20] Y. Zhu, T. Wang, T. Xu, Y. Li, C. Wang, Size effect of Pt co-catalyst on photocatalytic efficiency of g-C₃N₄ for hydrogen evolution, *Applied Surface Science*, 464 (2019) 36-42.
- [21] S. Cao, J. Jiang, B. Zhu, J. Yu, Shape-dependent photocatalytic hydrogen evolution activity over a Pt nanoparticle coupled g-C₃N₄ photocatalyst, *Physical Chemistry Chemical Physics*, 18 (2016) 19457-19463.
- [22] C. Zhang, F. Liu, Y. Zhai, H. Ariga, N. Yi, Y. Liu, K. Asakura, M. Flytzani-Stephanopoulos, H. He, Alkali-metal-promoted Pt/TiO₂ opens a more efficient pathway to formaldehyde oxidation at ambient temperatures, *Angewandte Chemie International Edition*, 51 (2012) 9628-9632.
- [23] F.F. Schweinberger, M.J. Berr, M. Döblinger, C. Wolff, K.E. Sanwald, A.S. Crampton, C.J. Ridge, F. Jäckel, J. Feldmann, M. Tschurl, Cluster size effects in the photocatalytic hydrogen evolution reaction, *Journal of the American Chemical Society*, 135 (2013) 13262-13265.
- [24] X. Geng, W. Sun, W. Wu, B. Chen, A. Al-Hilo, M. Benamara, H. Zhu, F. Watanabe, J. Cui, T.-p. Chen, Pure and stable metallic phase molybdenum disulfide nanosheets for hydrogen evolution reaction, *Nature communications*, 7 (2016) 1-7.
- [25] J. Xing, H.B. Jiang, J.F. Chen, Y.H. Li, L. Wu, S. Yang, L.R. Zheng, H.F. Wang, P. Hu, H.J. Zhao, H.G. Yang, Active sites on hydrogen evolution photocatalyst, *Journal of Materials Chemistry A*, 1 (2013) 15258-15264.
- [26] Y.H. Li, J. Xing, Z.J. Chen, Z. Li, F. Tian, L.R. Zheng, H.F. Wang, P. Hu, H.J. Zhao, H.G. Yang, Unidirectional suppression of hydrogen oxidation on oxidized platinum clusters, *Nature communications*, 4 (2013) 1-7.

- [27] J. Xing, Y.H. Li, H.B. Jiang, Y. Wang, H.G. Yang, The size and valence state effect of Pt on photocatalytic H₂ evolution over platinized TiO₂ photocatalyst, *International journal of hydrogen energy*, 39 (2014) 1237-1242.
- [28] G. Kresse, J. Furthmüller, Efficient iterative schemes for ab initio total-energy calculations using a plane-wave basis set, *Physical review B*, 54 (1996) 11169.
- [29] G. Kresse, J. Furthmüller, Efficiency of ab-initio total energy calculations for metals and semiconductors using a plane-wave basis set, *Computational materials science*, 6 (1996) 15-50.
- [30] J.P. Perdew, K. Burke, M. Ernzerhof, Generalized gradient approximation made simple, *Physical review letters*, 77 (1996) 3865.
- [31] H.J. Monkhorst, J.D. Pack, Special points for Brillouin-zone integrations, *Physical review B*, 13 (1976) 5188.
- [32] S. Grimme, J. Antony, S. Ehrlich, H. Krieg, A consistent and accurate ab initio parametrization of density functional dispersion correction (DFT-D) for the 94 elements H-Pu, *The Journal of chemical physics*, 132 (2010) 154104.
- [33] S. Grimme, S. Ehrlich, L. Goerigk, Effect of the damping function in dispersion corrected density functional theory, *Journal of computational chemistry*, 32 (2011) 1456-1465.
- [34] A.D. Becke, E.R. Johnson, A density-functional model of the dispersion interaction, *The Journal of chemical physics*, 123 (2005) 154101.
- [35] E.R. Johnson, A.D. Becke, A post-Hartree-Fock model of intermolecular interactions: Inclusion of higher-order corrections, *The Journal of chemical physics*, 124 (2006) 174104.
- [36] R.F. Bader, Atoms in molecules, *Accounts of Chemical Research*, 18 (1985) 9-15.
- [37] W. Tang, E. Sanville, G. Henkelman, A grid-based Bader analysis algorithm without lattice bias, *Journal of Physics: Condensed Matter*, 21 (2009) 084204.
- [38] A. Speltini, A. Scalabrini, F. Maraschi, M. Sturini, A. Pisanu, L. Malavasi, A. Profumo, Improved photocatalytic H₂ production assisted by aqueous glucose biomass by oxidized g-C₃N₄, *International Journal of Hydrogen Energy*, 43 (2018) 14925-14933.
- [39] B. Lin, H. An, X. Yan, T. Zhang, J. Wei, G. Yang, Fish-scale structured g-C₃N₄ nanosheet with unusual spatial electron transfer property for high-efficiency photocatalytic hydrogen evolution, *Applied Catalysis B: Environmental*, 210 (2017) 173-183.
- [40] L. Yang, J. Huang, L. Shi, L. Cao, Q. Yu, Y. Jie, J. Fei, H. Ouyang, J. Ye, A surface modification resultant thermally oxidized porous g-C₃N₄ with enhanced photocatalytic hydrogen production, *Applied Catalysis B: Environmental*, 204 (2017) 335-345.
- [41] H. Sun, X. Zhou, H. Zhang, W. Tu, An efficient exfoliation method to obtain graphitic carbon nitride nanosheets with superior visible-light photocatalytic activity, *International Journal of Hydrogen Energy*, 42 (2017) 7930-7937.

- [42] M.R. Gholipour, F. Béland, T.-O. Do, Post-calcined carbon nitride nanosheets as an efficient photocatalyst for hydrogen production under visible light irradiation, *ACS Sustainable Chemistry & Engineering*, 5 (2017) 213-220.
- [43] J. Lee, W. Choi, Photocatalytic reactivity of surface platinized TiO₂: substrate specificity and the effect of Pt oxidation state, *The Journal of Physical Chemistry B*, 109 (2005) 7399-7406.
- [44] F. Fina, H. Menard, J.T.S. Irvine, The effect of Pt NPs crystallinity and distribution on the photocatalytic activity of Pt-g-C₃N₄, *Physical Chemistry Chemical Physics*, 17 (2015) 13929-13936.
- [45] F. Fina, S.K. Callear, G.M. Carins, J.T. Irvine, Structural investigation of graphitic carbon nitride via XRD and neutron diffraction, *Chemistry of Materials*, 27 (2015) 2612-2618.
- [46] J. Fu, B. Zhu, C. Jiang, B. Cheng, W. You, J. Yu, Hierarchical porous O-doped g-C₃N₄ with enhanced photocatalytic CO₂ reduction activity, *Small*, 13 (2017) 1603938.
- [47] J. Ding, W. Xu, H. Wan, D. Yuan, C. Chen, L. Wang, G. Guan, W.-L. Dai, Nitrogen vacancy engineered graphitic C₃N₄-based polymers for photocatalytic oxidation of aromatic alcohols to aldehydes, *Applied Catalysis B: Environmental*, 221 (2018) 626-634.
- [48] Y. Zhou, W. Lv, B. Zhu, F. Tong, J. Pan, J. Bai, Q. Zhou, H. Qin, Template-free one-step synthesis of g-C₃N₄ nanosheets with simultaneous porous network and S-doping for remarkable visible-light-driven hydrogen evolution, *ACS Sustainable Chemistry & Engineering*, 7 (2019) 5801-5807.
- [49] D.Q. Dao, T.K.A. Nguyen, T.-T. Pham, E.W. Shin, Synergistic Effect on Photocatalytic Activity of Co-Doped NiTiO₃/g-C₃N₄ Composites under Visible Light Irradiation, *Catalysts*, 10 (2020) 1332.
- [50] L. Ma, H. Fan, K. Fu, S. Lei, Q. Hu, H. Huang, G. He, Protonation of graphitic carbon nitride (g-C₃N₄) for an electrostatically self-assembling carbon@ g-C₃N₄ core-shell nanostructure toward high hydrogen evolution, *ACS Sustainable Chemistry & Engineering*, 5 (2017) 7093-7103.
- [51] Y. Jiang, Z. Sun, C. Tang, Y. Zhou, L. Zeng, L. Huang, Enhancement of photocatalytic hydrogen evolution activity of porous oxygen doped g-C₃N₄ with nitrogen defects induced by changing electron transition, *Applied Catalysis B: Environmental*, 240 (2019) 30-38.
- [52] X. Du, G. Zou, Z. Wang, X. Wang, A scalable chemical route to soluble acidified graphitic carbon nitride: an ideal precursor for isolated ultrathin g-C₃N₄ nanosheets, *Nanoscale*, 7 (2015) 8701-8706.
- [53] J. Liu, M. Jiao, L. Lu, H.M. Barkholtz, Y. Li, Y. Wang, L. Jiang, Z. Wu, D.-j. Liu, L. Zhuang, High performance platinum single atom electrocatalyst for oxygen reduction reaction, *Nature communications*, 8 (2017) 1-10.

- [54] Z.-F. Huang, J. Song, L. Pan, Z. Wang, X. Zhang, J.-J. Zou, W. Mi, X. Zhang, L. Wang, Carbon nitride with simultaneous porous network and O-doping for efficient solar-energy-driven hydrogen evolution, *Nano Energy*, 12 (2015) 646-656.
- [55] X. She, L. Liu, H. Ji, Z. Mo, Y. Li, L. Huang, D. Du, H. Xu, H. Li, Template-free synthesis of 2D porous ultrathin nonmetal-doped g-C₃N₄ nanosheets with highly efficient photocatalytic H₂ evolution from water under visible light, *Applied Catalysis B: Environmental*, 187 (2016) 144-153.
- [56] S. Zhang, Y. Yang, Y. Guo, W. Guo, M. Wang, Y. Guo, M. Huo, Preparation and enhanced visible-light photocatalytic activity of graphitic carbon nitride/bismuth niobate heterojunctions, *Journal of hazardous materials*, 261 (2013) 235-245.
- [57] W. Zou, B. Deng, X. Hu, Y. Zhou, Y. Pu, S. Yu, K. Ma, J. Sun, H. Wan, L. Dong, Crystal-plane-dependent metal oxide-support interaction in CeO₂/g-C₃N₄ for photocatalytic hydrogen evolution, *Applied Catalysis B: Environmental*, 238 (2018) 111-118.
- [58] C.S. Kam, T.L. Leung, F. Liu, A.B. Djurišić, M.H. Xie, W.-K. Chan, Y. Zhou, K. Shih, Lead removal from water—dependence on the form of carbon and surface functionalization, *RSC Advances*, 8 (2018) 18355-18362.
- [59] D. Yang, A. Velamakanni, G. Bozoklu, S. Park, M. Stoller, R.D. Piner, S. Stankovich, I. Jung, D.A. Field, C.A. Ventrice Jr, Chemical analysis of graphene oxide films after heat and chemical treatments by X-ray photoelectron and Micro-Raman spectroscopy, *Carbon*, 47 (2009) 145-152.
- [60] B. Yu, X. Wang, X. Qian, W. Xing, H. Yang, L. Ma, Y. Lin, S. Jiang, L. Song, Y. Hu, Functionalized graphene oxide/phosphoramidate oligomer hybrids flame retardant prepared via in situ polymerization for improving the fire safety of polypropylene, *RSC Advances*, 4 (2014) 31782-31794.
- [61] M. Peuckert, H. Bonzel, Characterization of oxidized platinum surfaces by X-ray photoelectron spectroscopy, *Surface science*, 145 (1984) 239-259.
- [62] S. Strbac, S. Petrovic, R. Vasilic, J. Kovac, A. Zalar, Z. Rakocevic, Carbon monoxide oxidation on Au (1 1 1) surface decorated by spontaneously deposited Pt, *Electrochimica Acta*, 53 (2007) 998-1005.
- [63] B. Zhu, L. Zhang, B. Cheng, J. Yu, First-principle calculation study of tri-s-triazine-based g-C₃N₄: a review, *Applied Catalysis B: Environmental*, 224 (2018) 983-999.
- [64] X. Li, W. Bi, L. Zhang, S. Tao, W. Chu, Q. Zhang, Y. Luo, C. Wu, Y. Xie, Single-atom Pt as co-catalyst for enhanced photocatalytic H₂ evolution, *Advanced Materials*, 28 (2016) 2427-2431.
- [65] W. Xing, W. Tu, M. Ou, S. Wu, S. Yin, H. Wang, G. Chen, R. Xu, Anchoring Active Pt²⁺/Pt⁰ Hybrid Nanodots on g-C₃N₄ Nitrogen Vacancies for Photocatalytic H₂ Evolution, *ChemSusChem*, 12 (2019) 2029-2034.
- [66] M.-Y. Yen, C.-C. Teng, M.-C. Hsiao, P.-I. Liu, W.-P. Chuang, C.-C.M. Ma, C.-K. Hsieh, M.-C. Tsai, C.-H. Tsai, Platinum nanoparticles/graphene composite catalyst

- as a novel composite counter electrode for high performance dye-sensitized solar cells, *Journal of Materials Chemistry*, 21 (2011) 12880-12888.
- [67] Z. Teng, N. Yang, H. Lv, S. Wang, M. Hu, C. Wang, D. Wang, G. Wang, Edge-functionalized g-C₃N₄ nanosheets as a highly efficient metal-free photocatalyst for safe drinking water, *Chem*, 5 (2019) 664-680.
- [68] Y. Yu, W. Yan, X. Wang, P. Li, W. Gao, H. Zou, S. Wu, K. Ding, Surface engineering for extremely enhanced charge separation and photocatalytic hydrogen evolution on g-C₃N₄, *Advanced Materials*, 30 (2018) 1705060.
- [69] H. Li, Z. Zhang, Y. Liu, W. Cen, X. Luo, Functional group effects on the HOMO–LUMO gap of g-C₃N₄, *Nanomaterials*, 8 (2018) 589.
- [70] W. Zhang, Z. Zhang, S. Kwon, F. Zhang, B. Stephen, K.K. Kim, R. Jung, S. Kwon, K.-B. Chung, W. Yang, Photocatalytic improvement of Mn-adsorbed g-C₃N₄, *Applied Catalysis B: Environmental*, 206 (2017) 271-281.
- [71] Z. Zeng, X. Quan, H. Yu, S. Chen, W. Choi, B. Kim, S. Zhang, Alkali-metal-oxides coated ultrasmall Pt sub-nanoparticles loading on intercalated carbon nitride: Enhanced charge interlayer transportation and suppressed backwark reaction for overall water splitting, *Journal of Catalysis*, 377 (2019) 72-80.
- [72] F. Dong, Z. Zhao, T. Xiong, Z. Ni, W. Zhang, Y. Sun, W.-K. Ho, In situ construction of g-C₃N₄/g-C₃N₄ metal-free heterojunction for enhanced visible-light photocatalysis, *ACS applied materials & interfaces*, 5 (2013) 11392-11401.
- [73] Y. Wang, W. Yang, X. Chen, J. Wang, Y. Zhu, Photocatalytic activity enhancement of core-shell structure g-C₃N₄@TiO₂ via controlled ultrathin g-C₃N₄ layer, *Applied Catalysis B: Environmental*, 220 (2018) 337-347.
- [74] N. Yao, J. Huang, K. Fu, X. Deng, M. Ding, S. Zhang, X. Xu, L. Li, Reduced interfacial recombination in dye-sensitized solar cells assisted with NiO: Eu³⁺, Tb³⁺ coated TiO₂ film, *Scientific reports*, 6 (2016) 1-9.
- [75] K. Jiang, H. Jung, T.-T. Pham, D.Q. Dao, T.K.A. Nguyen, H. Yu, Y. Men, E.W. Shin, Modification of NiTiO₃ visible light-driven photocatalysts by Nb doping and NbO_x heterojunction: oxygen vacancy in the Nb-doped NiTiO₃ structure, *Journal of Alloys and Compounds*, (2021) 158636.
- [76] J. Feng, G. Liu, S. Yuan, Y. Ma, Influence of functional groups on water splitting in carbon nanodot and graphitic carbon nitride composites: a theoretical mechanism study, *Physical Chemistry Chemical Physics*, 19 (2017) 4997-5003.
- [77] C. Wu, Q. Han, L. Qu, Functional group defect design in polymeric carbon nitride for photocatalytic application, *APL Materials*, 8 (2020) 120703.
- [78] L. Chen, Y. Wang, C. Wu, G. Yu, Y. Yin, C. Su, J. Xie, Q. Han, L. Qu, Synergistic oxygen substitution and heterostructure construction in polymeric semiconductors for efficient water splitting, *Nanoscale*, 12 (2020) 13484-13490.
- [79] J.S. Jang, S.H. Choi, H.G. Kim, J.S. Lee, Location and state of Pt in platinized CdS/TiO₂ photocatalysts for hydrogen production from water under visible light, *The Journal of Physical Chemistry C*, 112 (2008) 17200-17205.

- [80] C. Xi, Z. Chen, Q. Li, Z. Jin, Effects of H^+ , Cl^- and CH_3COOH on the photocatalytic conversion of $PtCl_6^{2-}$ in aqueous TiO_2 dispersion, *Journal of Photochemistry and Photobiology A: Chemistry*, 87 (1995) 249-255.
- [81] K. Wenderich, G. Mul, Methods, mechanism, and applications of photodeposition in photocatalysis: a review, *Chemical reviews*, 116 (2016) 14587-14619.
- [82] X. Jiang, X. Fu, L. Zhang, S. Meng, S. Chen, Photocatalytic reforming of glycerol for H_2 evolution on Pt/ TiO_2 : fundamental understanding the effect of co-catalyst Pt and the Pt deposition route, *Journal of Materials Chemistry A*, 3 (2015) 2271-2282.
- [83] F. Zhang, J. Chen, X. Zhang, W. Gao, R. Jin, N. Guan, Y. Li, Synthesis of titania-supported platinum catalyst: the effect of pH on morphology control and valence state during photodeposition, *Langmuir*, 20 (2004) 9329-9334.
- [84] Y. Shi, Z.-R. Ma, Y.-Y. Xiao, Y.-C. Yin, W.-M. Huang, Z.-C. Huang, Y.-Z. Zheng, F.-Y. Mu, R. Huang, G.-Y. Shi, Electronic metal-support interaction modulates single-atom platinum catalysis for hydrogen evolution reaction, *Nature communications*, 12 (2021) 1-11.
- [85] M. Qureshi, A.T. Garcia-Esparza, G. Jeantelot, S. Ould-Chikh, A. Aguilar-Tapia, J.-L. Hazemann, J.-M. Basset, D. Loffreda, T. Le Bahers, K. Takanabe, Catalytic consequences of ultrafine Pt clusters supported on $SrTiO_3$ for photocatalytic overall water splitting, *Journal of Catalysis*, 376 (2019) 180-190.
- [86] X. Zhou, Y. Li, Y. Xing, J. Li, X. Jiang, Effects of the preparation method of Pt/g- C_3N_4 photocatalysts on their efficiency for visible-light hydrogen production, *Dalton Transactions*, 48 (2019) 15068-15073.
- [87] M. Luo, P. Lu, W. Yao, C. Huang, Q. Xu, Q. Wu, Y. Kuwahara, H. Yamashita, Shape and composition effects on photocatalytic hydrogen production for Pt-Pd alloy cocatalysts, *ACS applied materials & interfaces*, 8 (2016) 20667-20674.
- [88] L. Ma, H. Fan, J. Wang, Y. Zhao, H. Tian, G. Dong, Water-assisted ions in situ intercalation for porous polymeric graphitic carbon nitride nanosheets with superior photocatalytic hydrogen evolution performance, *Applied Catalysis B: Environmental*, 190 (2016) 93-102.
- [89] L. Ma, H. Fan, M. Li, H. Tian, J. Fang, G. Dong, A simple melamine-assisted exfoliation of polymeric graphitic carbon nitrides for highly efficient hydrogen production from water under visible light, *Journal of Materials Chemistry A*, 3 (2015) 22404-22412.
- [90] Q. Liang, Z. Li, Z.H. Huang, F. Kang, Q.H. Yang, Holey graphitic carbon nitride nanosheets with carbon vacancies for highly improved photocatalytic hydrogen production, *Advanced Functional Materials*, 25 (2015) 6885-6892.
- [91] Q. Han, B. Wang, J. Gao, Z. Cheng, Y. Zhao, Z. Zhang, L. Qu, Atomically thin mesoporous nanomesh of graphitic C_3N_4 for high-efficiency photocatalytic hydrogen evolution, *ACS nano*, 10 (2016) 2745-2751.
- [92] S. Guo, Z. Deng, M. Li, B. Jiang, C. Tian, Q. Pan, H. Fu, Phosphorus-doped carbon nitride tubes with a layered micro-nanostructure for enhanced visible-light photocatalytic hydrogen evolution, *Angewandte Chemie*, 128 (2016) 1862-1866.

- [93] Y. Chen, B. Lin, H. Wang, Y. Yang, H. Zhu, W. Yu, J.-m. Basset, Surface modification of g-C₃N₄ by hydrazine: simple way for noble-metal free hydrogen evolution catalysts, *Chemical Engineering Journal*, 286 (2016) 339-346.
- [94] V.H. Pham, T.T. Dang, K. Singh, S.H. Hur, E.W. Shin, J.S. Kim, M.A. Lee, S.H. Baeck, J.S. Chung, A catalytic and efficient route for reduction of graphene oxide by hydrogen spillover, *Journal of Materials Chemistry A*, 1 (2013) 1070-1077.
- [95] N. Kishner, Wolff–Kishner reduction; Huang–Minlon modification, *J. Russ. Phys. Chem. Soc.*, 43 (1911) 582-595.
- [96] L. Wolff, Chemischen institut der Universität Jena: methode zum ersatz des sauerstoffatoms der ketone und aldehyde durch wasserstoff.[Erste Abhandlung.], *Justus Liebigs Annalen der Chemie*, 394 (1912) 86-108.